Sag currents are a major contributor to human pyramidal cell intrinsic differences across cortical layers

Homeira Moradi Chameh[1], Scott Rich[1], Lihua Wang[9], Fu-Der Chen[8], Liang Zhang[2,9], Peter L. Carlen[2,9], Shreejoy J. Tripathy[3,4,5]*, Taufik A. Valiante[1,5,6,7,8]*

[1] *Krembil Research Institute, Division of Clinical and Computational Neuroscience*
[2] *Department of Physiology, University of Toronto*
[3] *Krembil Centre for Neuroinformatics, Centre for Addiction and Mental Health*
[4] *Department of Psychiatry, University of Toronto.*
[5] *Institute of Medical Sciences, University of Toronto.*
[6] *Department of Surgery, Division of Neurosurgery, University of Toronto*
[7] *Institute of Biomaterials and Biomedical Engineering, University of Toronto*
[8] *Electrical and Computer Engineering, University of Toronto*
[9] *Krembil Research Institute, Division of Experimental and Translational Neuroscience*
**Denotes equal contribution*

Abstract

In the human neocortex, coherent theta (~8Hz) oscillations between superficial and deep cortical layers are driven by deep layer neurons, suggesting distinct intrinsic electrophysiological properties of L5 neurons. We used in vitro whole-cell recordings to characterize pyramidal cells in layer 2/3 (L2/3), layer 3c (L3c) and layer 5 (L5) of the human neocortex. L5 pyramidal cells were more excitable and had a more prominent sag relative to L2/3 and L3c neurons that was abolished by blockade of the hyperpolarization activated cation current (I_h). We found a greater proportion of L5 and L3c neurons displaying subthreshold resonance relative to L2/3. Although no theta subthreshold resonance was observed in either L5 and L2/3 neurons, L5 neurons were more adept at tracking both delta (4Hz) and theta oscillations, the former being dependent on I_h. The unique features of human L5 neurons likely contribute to the emergence of theta oscillations in human cortical microcircuits.

1. Introduction

Comparative studies between human and rodent cortical neuronal physiology have revealed unique human cortical neuronal and microcircuit properties. At the cellular level, human neurons have been shown to have unique morphological properties [1], reduced membrane capacitances [2], increased dendritic compartmentalization in thick-tufted layer 5 (L5) pyramidal cells [3], higher h-channel densities in layer 3 (L3) versus layer 2 (L2) pyramidal cells [4], and a wholly unique interneuron cell type [5,6]. At the microcircuit level, human neocortical circuits demonstrate unique reverberant activity [7], different short-term plasticity rules, compared to neocortical circuits in rodents [8,9], and coherent oscillations between superficial and deep cortical layers [10]. In addition, correlations between patient IQ and cellular features of human layer 2, 3 and 4 pyramidal cells have been demonstrated in both action potential kinetics and the length and complexity of dendritic arbors [11].

Although understanding the unique biophysical and synaptic properties of neurons remains an important endeavor, computational models and mathematical formulations of neurons and circuits are essential for describing and explaining mesoscopic level collective dynamics such as oscillations [12-14]. Indeed, it has been recently posited that "a set of ***brain simulators*** based on ***neuron models*** at different

levels of biological detail" are needed in order to "allow for systematic refinement of candidate network models by comparison with ***experiments***"[15]. By extension, to create simulations of the human brain and cortical microcircuit, we need neuronal models derived from direct human experiments. Thus, as we explore what is uniquely human about the human brain in order to, for example, tackle the increasing societal burden of neurological and neuropsychiatric conditions [16,17], infusing computational models with human derived micro- and mesoscopic cellular and circuit properties will be critically important.

In this context, our previous experiments in human cortical slices have demonstrated that spontaneous theta-like activity, the most ubiquitous oscillatory frequency in the human brain [18], can be induced by application of cholinergic and glutamatergic agonists [10]. We observed theta oscillations that were coherent between cortical laminae, with the deep layer leading in phase relative to the superficial layer [10]. We also observed robust cross-frequency coupling between theta and high-gamma activity that was modulated with the strength of synchrony between cortical laminae [19]– "so called coordination though coherent phase–amplitude coupling"[20]. Given the role of intrinsic electrophysiological properties in the generation of oscillations [21] and our previous findings that deep layer theta leads superficial layer theta in phase, we reasoned that deep layer neurons in the human neocortex are likely endowed with distinct biophysical properties that enable them to "drive" such interlaminar activity.

One of the candidate membrane currents thought to contribute to low-frequency (< 8Hz) oscillations is the hyperpolarization activated cation current or h-current (I_h) [3,4,22,23]. This current is important for oscillations and pacemaking activity in a myriad of cell types, ranging from thalamic and hippocampal neurons to cardiac pacemaker neurons [24,25]. Consistent with its role in contributing to resonant activity, in a recent study in the human neocortex Kalmbach, B et. al (2018) demonstrated a prominent sag voltage in deep L3 versus superficial L2 neurons, and further, that I_h appeared necessary for the resonance observed in the L3 neurons [4]. In addition, it has recently been reported that thick-tufted neurons in L5 of the human neocortex also display prominent somatic and dendritic I_h and subthreshold resonance [3].

Based on our previous findings demonstrating that deep layer activity appears to drive superficial activity, we hypothesized that intrinsic pyramidal cell properties would differ between deep versus superficial layers. We used whole-cell recordings to characterize pyramidal cells in L2/3, L3c, and L5, focusing in particular on the amplitude and kinetics of I_h or sag voltage. In addition to key biophysical differences favoring greater excitability in human L5 vs. L2/3 pyramidal cells, we found that L5 and L3c demonstrated larger sag voltage amplitudes relative to L2/3 pyramidal cells. Somewhat surprisingly, while some subthreshold theta resonance was observed in our experiments, we found this feature to be generally quite rare amongst pyramidal cells across all layers. However, we observed that L5 pyramidal cells showed enhanced frequency dependent gain at delta and theta frequencies. Lastly, we found a great deal of cell-to-cell variability in electrophysiological parameters sampled from pyramidal cells recorded within the same lamina, and that this variability is especially large in L5.

2. Materials and Methods

2.1. Human brain slice preparation

Written informed consent was obtained from all study participants as stated in the research protocol. In accordance with the Declaration of Helsinki, approval for this study was received by the University Health Network Research Ethics board. Sixty-one patients, age ranging between 19 to 63 years (Mean age: 37.1 ± 1.8), underwent a standard anterior temporal lobectomy (ATL) [26] or tumor resection from the frontal or temporal lobe [27,28] under general anesthesia using volatile anesthetics.

The surgery involved resecting the first 4.5 cm of neocortex using sharp dissection and local cooling with ~4 °C TissueSol®. Immediately following surgical resection, the cortical block was submerged in an ice-cold (~4°C) cutting solution that was continuously bubbled with 95% O_2-5% CO_2 containing (in mM) sucrose 248, KCl 2, $MgSO_4.7H_2O$ 3, $CaCl_2.2H_2O$ 1, $NaHCO_3$ 26, $NaH_2PO_4.H_2O$ 1.25, D-glucose 10. The osmolarity was adjusted to 300-305 mOsm. The total duration, including slicing and transportation, was kept to a maximum of 20 minutes [28]. Transverse brain slices (400 µm) were obtained using a vibratome (Leica 1200 V) in cutting solution. Tissue slicing was performed perpendicular to the pial surface to ensure that pyramidal cell dendrites were minimally truncated [4,27]. The cutting solution was the same as used for transport of tissue from operation room to the laboratory. After sectioning, the slices were incubated for 30 min at 34 °C in standard artificial cerebrospinal fluid (aCSF) (in mM): NaCl 123, KCl 4, $CaCl_2.2H_2O$ 1, $MgSO_4.7H_2O$ 1, $NaHCO_3$ 26, $NaH_2PO_4.H_2O$ 1.2, and D-glucose 10, pH 7.40. All aCSF and cutting solutions were continuously bubbled with carbogen gas (95% O_2-5% CO_2) and had an osmolarity of 300-305 mOsm. Following this incubation, the slices were maintained in standard aCSF at 22–23 °C for at least 1 h, until they were individually transferred to a submerged recording chamber.

For a subset of experiments designed to assess frequency dependent gain, slices were prepared using the NMDG protective recovery method [29]. The slicing and transport solution was composed of (in mM): NMDG 92, KCl 2.5, NaH_2PO_4 1.25, $NaHCO_3$ 30, HEPES 20, Glucose 25, Thiourea 2, Na L-ascorbate 5, Na-Pyruvate 3, $CaCl_2.4H_2O$ 0.5, and $MgSO_4.7H_2O$ 10. The pH of NMDG solution was adjusted to 7.3-7.4 using hydrochloric acid and the osmolarity was 300-305 mOsm. Before transport and slicing, the NMDG solution was carbogenated for 15 min and chilled to 2-4 °C. After slices were cut (as described above), they were transferred to a recovery chamber filled with 32-34 °C NMDG solution, and continuously bubbled with 95% O_2 5% CO_2. After 12 minutes, the slices were transferred to an incubation solution containing (in mM): NaCl 92, KCl 2.5, $NaH_2PO_4.H_2O$ 1.25, $NaHCO_3$ 30, HEPES 20, Glucose 25, Thiourea 2, Na L-ascorbate 5, Na-Pyruvate 3, $CaCl_2.4H_2O$ 2, and $MgSO_4.7H_2O$ 2. The solution was continuously bubbled with 95% O_2 -5% CO_2. After a 1 hour incubation at room temperature, slices were transferred to a recording chamber and continuously perfused with aCSF containing (in mM): NaCl 126, KCl 2.5, $NaH_2PO_4.H_2O$ 1.25, $NaHCO_3$ 26, Glucose 12.6, $CaCl2.2H_2O$ 2, and $MgSO_4.7H_20$ 1. We emphasize that these experiments were performed with excitatory (APV 50 µM, Sigma; CNQX 25 µM, Sigma) and inhibitory (Bicuculline 10 µM, Sigma; CGP-35348 10 µM, Sigma) synaptic activity blocked. These blockers are only used in these experiments, highlighted in Figure 5.

2.2. Electrophysiology recordings and intrinsic physiology feature analysis

For recordings, slices were transferred to a recording chamber mounted on a fixed-stage upright microscope (Olympus BX_{51}WI upright microscope; Olympus Optical Co., NY, USA and Axioskop 2 FS MOT; Carl Zeiss, Germany). Slices were continually perfused at 4 ml/min with standard aCSF at 32-34 °C. Cortical neurons were visualized using an IR-CCD camera (IR-1000, MTI, USA) with a 40x water immersion objective lens. Using the IR-DIC microscope, the boundary between layer 1 and 2 was easily distinguishable in terms of cell density. Below L2, the sparser area of neurons (L3) were followed by a tight band of densely packed layer 4 (L4) neurons. L4 was followed by a decrease in cell density (L5). In general, we did not annotate different neurons recorded from L2 versus those recorded from L3, except when explicitly mentioned.

Patch pipettes (3-6 MΩ resistance) were pulled from standard borosilicate glass pipettes (thin-wall borosilicate tubes with filaments, World Precision Instruments, Sarasota, FL, USA) using a vertical puller (PC-10, Narishige). Pipettes were filled with intracellular solution containing (in mM): K-gluconate 135; NaCl 10; HEPES 10; $MgCl_2$ 1; Na_2ATP 2; GTP 0.3, pH adjusted with KOH to 7.4 (290–309 mOsm). In a subset of experiments the pipette solution also contained biocytin (3-5%). Whole-cell patch-clamp recordings were obtained using a Multiclamp 700A amplifier, Axopatch 200B amplifier, pClamp 9.2 and pClamp 10.6 data

acquisition software (Axon instruments, Molecular Devices, USA). Subsequently, electrical signals were digitized at 20 kHz using a 1320X digitizer. The access resistance was monitored throughout the recording (typically between 8-25 MΩ), and neurons were discarded if the access resistance was > 25 MΩ. The liquid junction potential was calculated to be -10.8 mV and was not corrected.

Data were analysed off-line using Clampfit 10.7, Python, MATLAB, and R software. The resting membrane potential (RMP) was measured after breaking into the cell (IC=0). The majority of the intrinsic electrophysiological features reported here were calculated using the Python IPFX toolbox (https://github.com/AllenInstitute/ipfx/) with default parameter settings [30]. The input resistance and membrane time constant were calculated using hyperpolarizing sweeps between -50 to -200pA. Single action potential features, the like action potential threshold, peak, width at half-max, and the upstroke-downstroke ratio, were calculated using the first spike at rheobase. The adaptation index, average firing rate, inter-spike intervals (first, mean, median, coefficient of variation) were defined using the "hero" sweep with default parameters (defined as the sweep between 39 to 61 pA greater than the rheobase). Sag amplitude and sag ratio were defined in response to hyperpolarizing current pulses (600ms duration, 0 to -400 pA, 50 pA steps). The sag ratio was calculated as the difference between the minimum value and the steady state divided by peak deflection during hyperpolarization current injection. The rebound depolarization amplitude was calculated as the difference between the steady state voltage and the maximum depolarization potential. We also observed the presence or absence of rebound spiking following the injection of hyperpolarization current steps (-400 pA). The I_h blocker ZD7288 (10 μM, Sigma Aldrich) was applied to confirm pharmacological evidence for I_h.

Bursting neurons were defined as those where the instantaneous frequency (determined by the first inter-spike interval at rheobase) was greater than 75 Hz. We identified putative interneurons within our dataset by manually assessing each cell's maximum firing rates, spike widths, and after-hyperpolarization amplitudes. Interneurons typically had spike half-widths less than <1 ms, afterhyperpolarization amplitudes greater than 10 mV, and maximum firing rates > 75Hz [31].

2.3. Voltage-clamp characterisation of I_h and I_{tail}

To characterize the I_h, 600 ms-long voltage-clamp steps were used in -10mV increments, down to -140mV from a holding potential of -60mV. In order to measure I_h amplitude, the difference between the steady state at the end of the holding potential and the maximum current was determined. The I_{tail} was quantified as the difference between peak amplitude of residual current at the end of each holding potential and the steady state current from holding potentials of -140 to -60 mV. A single or double-exponential model, fitted to the various currents recorded, was used to calculate the time constants of I_h in order to determine the kinetics of I_h. To measure the voltage sensitivity of I_h in L2/3 and L5 pyramidal cells, the membrane potential evoking half-maximal activation of I_h (V_{50}) was obtained by fitting the I_h activation to a Boltzmann sigmoid function using GraphPad 6 (GraphPad, San Diego, CA, USA). In experiments to quantify I_h, the sodium channel blocker tetrodotoxin (1 μM; Alomone Labs) to block voltage gated sodium currents, $CoCl_2$ (2mM; Sigma-Aldrich) to block voltage-sensitive calcium currents, and $BaCl_2$ (1mM; Sigma-Aldrich) to block inwardly rectifying potassium current were added to the bath solution. We note that space clamp issues limit the precise quantification of the I_h [32].

2.4. Subthreshold resonance and spike probability analyses

To assess the subthreshold and suprathreshold resonance properties, a frequency modulated sine wave current input (ZAP/chirp) was generated ranging from 1 to 20Hz, lasting 20s [33] with a sampling rate of 10kHz. This current waveform was then injected using the custom waveform feature of Clampex 9.2 and

Clampex 10.2 (Axon Instruments, Molecular devices, USA). The subthreshold current amplitude was adjusted to the maximal current that did not elicit spiking.

For determining subthreshold resonance, only trials without spiking were utilized for analysis. Analyses were performed using in house Python scripts adapted from [4]. The impedance profile of the cell was computed by taking the ratio of the voltage over current in the frequency domain obtained with the fast Fourier transform. Window averaging was then applied to smooth the impedance profile of the cell. The impedance profiles were then averaged over several trials (up to 5) to obtain the mean impedance profile of the cell. The frequency point with the highest impedance is the center frequency while the frequency point with half of the center impedance is the 3dB cut-off frequency. Resonant neurons were defined as those with resonant frequencies greater than 0.5 Hz, the lowest frequency tested here.

To analyze responses to suprathreshold frequency-modulated sinusoidal current, spiking probability as a function of input frequency was assessed using suprathreshold current stimulation. The suprathreshold current was set by gradually increasing the amplitude of the ZAP function input by adjusting the gain of the stimulus until the first spike was elicited. Ten traces per cell were utilized to obtain the probability of spiking as a function of frequency. Since the instantaneous frequency is known from the current input, each action potential could be assigned a frequency at which it occurred. To create the spike probability density function for each cell type, the frequencies at which individual spikes occurred were pooled, a histogram generated and divided by the total number of spikes. To compare spike probability density functions between cell types the distributions were compared using a two-sample Kolmogorov-Smirnov test (`kstest2.m`).

2.5. Multi-variate electrophysiological feature analysis

We used a dimensionality reduction approach to visualize similarities in recorded neurons according to multi-variate correlations in measured electrophysiology features. We specifically used the uniform manifold approximation (UMAP) function and library implemented in R with default parameter settings [34]. We defined each recorded cell using feature vectors constructed from a set of 14 electrophysiological features that were reliably calculated in most characterized neurons. We specifically used the following subthreshold features: resting membrane potential, input resistance, membrane time constant, sag ratio, sag amplitude. We additionally used the following suprathreshold features of the first action potential at rheobase: AP threshold, amplitude, half-width, upstroke-downstroke ratio, after-hyperpolarization amplitude, rheobase, and latency to first spike. We also used the following spike train features: slope of FI curve and average spiking rate at the hero sweep stimulus.

2.6. Frequency Dependent Gain

Following a similar methodology of [35], frequency dependent gain was computed using 30 trials (inter-trial interval = 20s) of a 2.5s duration current injection stimulus of frozen white noise convolved with a 3ms square function [36]. The amplitude (a.k.a. variance) of the current injection stimulus was scaled to elicit spike rates of above 5 Hz, the typical firing rate for cortical pyramidal cells [37]. In addition to increasing the noise variance, a steady amount of DC current was required [35] to elicit spiking, which was delivered as various amplitude steps were added to the noisy current input. Peaks detected in the voltage time series with overshoot greater than 0 mV were taken to be the occurrence of an action potential. The time varying firing rate *r(t)* was given by:

$$r(t) = \begin{cases} \frac{1}{\Delta t} & where\ spike\ detected \\ 0 & Where\ no\ spike\ detected \end{cases}$$

The stimulus–response correlation (c_{sr}) and the stimulus autocorrelation (c_{ss}) were calculated in the following fashion:

$$c_{sr}(\tau) = \langle s(t)r(t+\tau)\rangle$$

$$C_{ss}(\tau) = \langle s(t)s(t+\tau)\rangle$$

where τ is the time difference, and the stimulus $s(t)$ is $I_{noise}(t)$. After windowing the $c_{sr}(\tau)$ and $c_{ss}(\tau)$ functions (see below), the complex Fourier components $C_{sr}(f)$ and $C_{ss}(f)$ were obtained, and the frequency-dependent gain and the average phase shift were calculated with $\sigma = 1/f$, in order to ensure the spectral estimates were not dominated by noise. The gain (G(f)) and the phase ($\varphi(f)$) are:

$$G(f) = \frac{|C_{sr}(f)|}{|C_{ss}(f)|}$$

$$\varphi(f) = atan\frac{[Im[C_{sr}(f)]]}{[Re[C_{sr}(f)]]}$$

where *Re* and *Im* refer to the real and imaginary parts of each Fourier component. $\varphi(f)$ was then corrected using the peak time (τ_{delay}) of $c_{sr}(\tau)$ [35].

For statistical testing, individual gains or *G(f)*s for each cell (30 trials/cell) from neurons with spike rates above 5 Hz were pooled for each cell type. To compare between cell types, Mann-Whitney U (`ranksum.m`) was used to obtain a *p*-value at each frequency (2-100Hz in 0.2Hz steps). The *p*-values were the false discovery rate corrected with an alpha = 0.01 [38].

2.7. Histological methods

During electrophysiological recording, biocytin (3-5 mg/ml) was allowed to diffuse into the patched neuron; after 20-45 min, the electrodes were slowly retracted under visual guidance to maintain the quality of the seal and staining. The slices were left for another 10-15 min in the recording chamber to washout excess biocytin from extracellular space, then transferred to 4% paraformaldehyde and kept at 4°C for 24 hours.

Subsequently, the slices were washed and transferred into PBS solution (0.1 mM). To reveal biocytin, slices were incubated in blocking serum (0.5 % Bovine serum albumin (BSA), 0.5 % milk powder) and 0.1% Triton X-100 in PBS for 1 hour at room temperature. Finally, slices were incubated with streptavidin-conjugated Alexa Fluor 568 (1:300) overnight at 4°C. Then slices were rinsed with PBS and mounted on the slide using moviol (Sigma-Aldrich). Imaging was done using a Zeiss LSM710 Multiphoton microscope. Reconstructions were performed using IMARIS software (Bitplane, Oxford instrument company).

2.8. Statistical analyses

Statistical analyses and plotting were performed using GraphPad Prism 6. Data are presented in the text as mean ± SD unless otherwise noted. Unless stated otherwise, a standard threshold of $p<0.05$ was used to report statistically significant differences. The Kruskal-Wallis test, a non-parametric test, was used to test for statistical differences among groups. Dunn's test was used to correct multiple comparisons. The non-parametric Mann-Whitney test was used to determine statistical differences between two groups.

To evaluate the presence of correlations between electrophysiological variables and patient demographic variables, we used a mixed effects modeling approach, implemented in R using lme4 [39].

Specifically, we modeled age as a fixed effect and patient ID as a random effect, i.e., ephys_prop ~ age + (1|subject_id). To evaluate the statistical significance of the demographic term, we fit a second model with the random effect only and used an ANOVA to evaluate the difference between the two models. To calculate correlation coefficients from mixed effects models for fixed effects terms (like age), we used the MuMIn R package to calculate the R squared values associated with our fixed effects (i.e., the marginal effect) and calculated the square root of this to obtain a correlation coefficient [40].

2.9. Data and code availability

Processed datasets will be made available upon reasonable request. Computational code for custom analyses are available at the following GitHub repositories: https://github.com/stripathy/valiante_ih (R) and https://github.com/stripathy/valiante_lab_abf_process (Python).

Table 1: Demographic data (for a subset of 49 patients where such information was available)

Age (Years)	Sex	Years of seizure history	Diagnosis	Antiepileptic drugs	Resection location
39	F	11	Tumor	LSC, LRZ, LEV	Right-ATL
58	F	8	Tumor	CBZ	Left-FL
57	M	45	Epilepsy	LSC, CZP, CBZ	Right-ATL
27	M	11	Epilepsy	LSC, LRZ, CLB	Right-ATL
24	M	8	Epilepsy	LEV, LTG	Right-ATL
25	M	12	Epilepsy	CBZ, LSC	Right-ATL
33	F	4	Epilepsy	LEV	Left-FL
33	M	14	Epilepsy	PHN, LEV	Right-FL
22	M	6	Epilepsy	PHN, CBZ, LTG	Left-ATL
21	M	2	Epilepsy	DR, CLB, MJ	Parietal lobe
22	M	12	Epilepsy	PHN, LRZ	Right-ATL
23	F	23	Epilepsy	CBZ, LEV, LSC	Right-FL
53	F	43	Epilepsy	CBZ, LSC, LEV	Left-ATL
37	F	2	Tumor	GPN, LSC, LEV, CLB, LRZ	Right-FL
47	F	4	Epilepsy	CBZ, CLB	Left-ATL
52	M	13	Epilepsy	CBZ, CLB	Left-ATL
50	F	26	Epilepsy	PHN, LTG	Right-ATL
36	F	34	Epilepsy	LSC, CBZ	Left-ATL
40	M	29	Epilepsy	LEV	Right-ATL
25	F	10	Epilepsy	CBZ, LSC, LEV	Right-ATL
52	M	27	Epilepsy	LSC, LRZ	Left-ATL
21	M	11	Epilepsy	LTG, CBZ	Left-ATL
63	M	0.1	Tumor	PHN	Right-Parietal
42	M	22	Epilepsy	CBZ	Right-FL
25	F	22	Epilepsy	LSC, CLB, LTG	Right-FL
24	F	3	Tumor	LEV	Left-ATL
53	M	9	Epilepsy	LEV	Left-ATL
45	F	20	Epilepsy	LTG	Right-ATL
26	F	25	Epilepsy	CBZ, CLB, LTG	Right-ATL
35	F	14	Epilepsy	LRZ, DR, PHN	Left-ATL
24	M	6	Epilepsy	LSC, LRZ, MJ	Right-ATL
53	F	51	Epilepsy	LSC, CLB	Left-ATL
44	F	3	Epilepsy	LTG	Left-ATL
25	M	14	Epilepsy	CBZ	Right-ATL
19	F	15	Epilepsy	PB, CLB, GPN, RFM	Right-ATL
30	M	12	Epilepsy	PHN	Left-ATL
26	M	5	Epilepsy	CBZ, DR	Right-ATL
28	M	13	Epilepsy	CLB, MJ	Left-ATL
52	F	6	Epilepsy	LTG, LEF	Left-ATL
26	F	9	Epilepsy	ESL, TMP, CLB	Right-ATL
59	F	39	Epilepsy	CLB, LSC	Right-ATL
37	M	5	Epilepsy	CLB, LSC	Right-ATL
55	M	27	Epilepsy	CLB, ESL, LTG	Left-ATL
42	F	3	Epilepsy	CBZ, GPN	Right-ATL
57	F	56	Epilepsy	CLB, LTG, PRM, CBD oil	Left-ATL
24	M	4	Epilepsy	LEV, LTG	Left ATL
33	M	6	Epilepsy	LSC, PGB, PHN	Right-ATL
39	M	12	Epilepsy	CLB, LTG, MJ	Left-ATL
36	F	16	Epilepsy	LSC, PGB, PHN	Right-ATL

CBZ, Carbamazepine; CLB, Clobazam; CZP, Clonazepam; DR, Divalproex; GPN, Gabapentin; LEV, Levetiracetam; LRZ, Lorazepam; LSC, Lacosamide; LTG, Lamotrigine; MJ, Marijuana; PB, Phenobarbital; PHN, Phenytoin; RFM, Rufinamide; LEF, Leflunomide; ESL, Eslicarbazepine Acetate; TMP, Tetramethylpyrazine; PRM, primidone; CBD, cannabidiol; PGB, Pregabalin.

3. Results

Whole-cell patch clamp recordings were obtained from human neocortical neurons located in L2/3, L3c and L5 within acute brain slices collected from 61 patients. Tissues were obtained from patients who underwent resective surgery for pharmacologically intractable epilepsy or tumor removal (a summary table with patient details shown in Supplemental Table 1). For many of our recordings, we did not annotate our L2/3 pyramidal cells as specifically belonging to either L2 or L3, considering the majority of these data were collected prior to publication of a recent paper illustrating divergent electrophysiological and morphological features of these neurons in the human neocortex [4]. Consequently, we later recorded from a targeted set of pyramidal cells in L3c (i.e., the deepest part of L3) to specifically contrast and compare our findings with those from previous finding [4].

3.1. Diverse morphologies and passive membrane properties of pyramidal cells in L2/3, L3c and L5

In order to confirm the successful targeting of pyramidal cells, a subset of neurons was filled with biocytin and underwent subsequent morphological reconstruction. Figure 1A shows example electrophysiological recordings of L2/3, L3c and L5 pyramidal cells with corresponding 3D morphological reconstructions.

The 3D reconstructions revealed a rich diversity of human pyramidal cell morphologies, consistent with recent detailed demonstrations of the distinct cellular morphologies of human cortical neurons as a function of the cortical lamina [1,3,4,41]. Pyramidal cells with somas located in L2 and the upper part of L3 had complex basal dendrites, with apical dendrites often reaching L1. Pyramidal cells located in L3c showed different morphologies, with one cell (cell d) showing simple basal dendrites and another (cell e) showing much more complex basal dendrites, consistent with recent reports on the heterogeneity of pyramidal cells in L3 [41]. Lastly, we observed two L5 neurons with very different morphologies: one cell (cell f) displays a simple, “thin-tufted” morphology with apical dendrites terminating at the border of L3 and L4, and another pyramidal cell (cell g) appears “thick-tufted” (similar to those reported in [3]), with a highly complex basal dendrite and two apical dendrite trunks, with one trunk terminating in upper L3 and the other projecting to lower L3 prior to being truncated due to slicing or optical truncation.

We next assessed the passive membrane properties (i.e. resting membrane potential, input resistance and membrane time constant) of human cortical pyramidal cells in L2/3, L3c and L5 (n=56, n=15 and n=105 neurons, respectively), using hyperpolarizing current steps in current-clamp mode (see Methods). We found that passive membrane properties differed significantly between pyramidal cells of L2/3, L3c and L5. We found that L3c and L5 neurons had more depolarized resting membrane potentials relative to L2/3 neurons (L2/3: -68.2 ± 5.3 mV, L3c: -65.6 ± 3.8 mV, L5: -65.6 ± 6.5mV; Figure 1B), with L5 neurons being significantly more depolarized at rest compared to L2/3 neurons (p=0.007). We also found that L5 pyramidal cells showed higher input resistances relative to L2/3 and L3c neurons (L2/3: 83± 38.1 MΩ, L3c:79.4 ± 21.4 MΩ, L5: 94.2 ± 41.3 MΩ; Figure1C). However, this difference was not significant between layers (p=0.1). L5 and L3c pyramidal cells also had slower membrane time constants (τ_m) compared to L2/3 (L2/3: 13.7 ± 7.1 ms, L3c: 17.1 ± 5.7 ms, L5: 19.3 ± 9.1 ms, p<0.0001; Figure 1D).

In general, we found considerable electrophysiological heterogeneity among neurons sampled within each cortical layer, broadly consistent with the morphological reconstructions shown in Fig 1A. For example, we found that pyramidal cells in L5 had input resistances as low as 20 MΩ and as high as 200 MΩ, likely reflecting the dichotomy or graded variation between thin- and thick-tufted pyramidal cells (as well as the potential of inadvertent cutting of dendrites during slice preparation, see Discussion). We note that the average input resistance among our population of recorded L5 pyramidal cells is considerably higher

than that reported in [3], likely arising from differences in the neurons targeted for recordings between our studies (see Discussion).

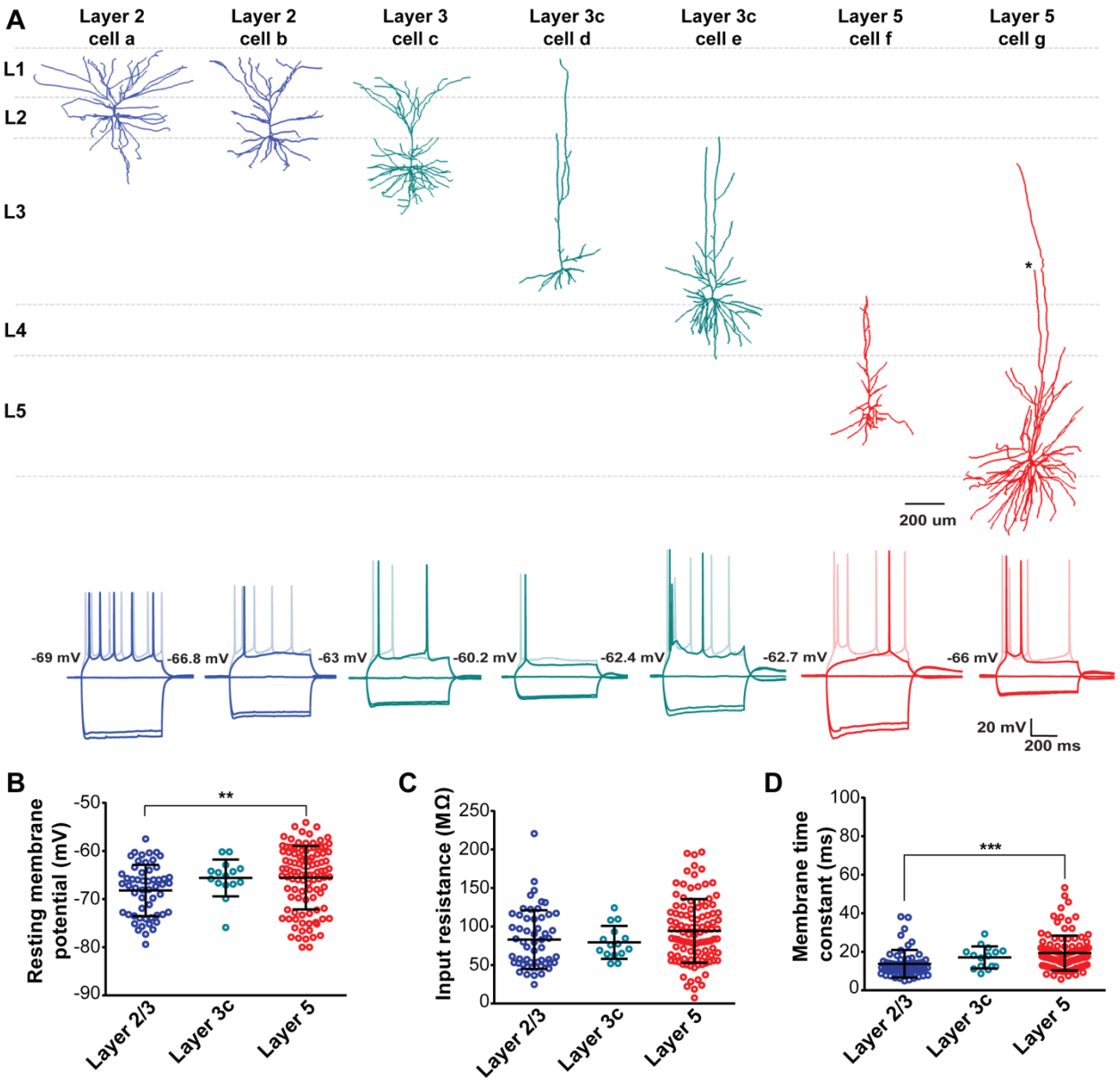

Figure 1. Diverse morphologies and passive membrane properties among pyramidal cells in the human neocortex. (A) Example 3D reconstructions (top) and voltage traces (bottom) for example L2/3, L3c and L5 pyramidal cells following hyperpolarizing and depolarizing current injection. Voltage traces have been shaded for visual clarity. Cortical layer and relative position from pial surface are annotated for each reconstructed cell. Asterisk in one branch of apical dendrite in cell g indicates truncation (dendrite morphologies were otherwise not visibly truncated). Cell e was recorded in the presence of blockers of synaptic activity (see Methods). **(B-D)** Resting membrane potentials (B), input resistances (C) and membrane time constants (C) for pyramidal cells in L2/3, L3c, and L5. Error bars in B-D denote mean and standard deviations (SD) and group comparisons and asterisks indicate significant group differences. ** denotes $p < 0.01$ and *** denotes $p < 0.001$, Wilcoxon non-parametric test.

3.2. Subthreshold active membrane properties of pyramidal cells in L2/3, L3c and L5

We next injected a series of hyperpolarizing currents to assay sag voltage and rebound depolarization (L2/3: n=56, L3c: n= 15, L5: n=105). L5 pyramidal cells had significantly larger sag voltage amplitudes than L2/3 pyramidal cells (L2/3: 1.7 ± 1.1 mV, L3c: 2.3 ± 0.7 mV, L5: 3.2 ± 1.9 mV, p<0.0001 between L2/3 and L5; Figures 2A, B). Our findings further support recent evidence for a positive correlation between sag voltage amplitude and distance from pial surface [4]. We found similar results using the dimensionless sag ratio measure, that normalizes for input resistance differences between neurons (Figure S1A). In addition, 21.9% of L5 pyramidal cells exhibited rebound spiking following the termination of a hyperpolarizing current pulse, whereas 1.8 % of L2/3 neurons exhibited rebound spiking and rebound spiking was not observed in any of the recorded L3c pyramidal cells. The rebound depolarization amplitude was significantly larger in L5 pyramidal cells compared to L2/3 and L3c neurons (L2/3: 1.8 ± 1. 6mV, L3c: 2.9 ± 1.8, L5: 4.2 ± 3 mV, p<0.0001 between L2/3 and L5; Figure 2C).

To further characterize the I_h specific component of membrane sag voltage, we bath applied the specific I_h blocker, ZD7288 (10 µm; ZD), with example traces shown in Figure 2D. For L2/3 (n=13), L3c (n=4) and L5 (n=10) pyramidal cells, after bath-applying ZD we observed a significant reduction in voltage sag amplitude (L2/3: before 1.3 ± 0.9 mV, after 0.2 ± 0.3 mV, p=0.0005, L3c: before 2.4 ± 1.4 mV, after 0.9 ± 0.9 mV, P=0.1, L5: before 3.1 ± 2.8 mV, after 0.9 ± 0.8 mV, p=0.002; Figure 2E) and in sag ratio (Figure S1B). Bath applying ZD7288 also significantly reduced the rebound depolarization amplitude (L2/3: before 1.3 ± 1.1 mV, after -0.8 ± 1.5 mV, p=0.001, L3c: before 3 ± 2.3 mV, after 0.9 ± 1.6 mV, p=0.1, L5: before 2.1 ± 1.9 mV, after -1.2 ± 2.3 mV, p=0.002; Figure 2F).

Whole-cell voltage-clamp experiments were performed in a subset of neurons (L2/3: n= 6, L5: n= 10) to determine if the I_h amplitude differences arose from differences in channel kinetics between these two cell-types. While space-clamp issues limit our ability to adequately voltage clamp distal cellular processes [32], we nevertheless considered it potentially beneficial to use this technique to obtain semi-quantitative estimates of the amplitudes, kinetics, and voltage dependence of the I_h in human pyramidal cells. We used pharmacological blockers to specifically isolate I_h (see Methods). We found that injecting voltage steps from -60 to -140 mV produced a slowly activating, inward current (example traces shown in Figure S2A). Consistent with our current clamp based results, we found that the amplitudes of the I_h were significantly smaller in L2/3 neurons compared with L5 (Figure S2C), whereas the time course of I_h activation and the voltage sensitivity of I_h (quantified at the half maximal activation voltage) was similar between L2/3 and L5 neurons (Figure S2B-D). These results suggest that the relatively larger L5 sag amplitude arises from increased channel numbers, rather than differences in channel kinetics.

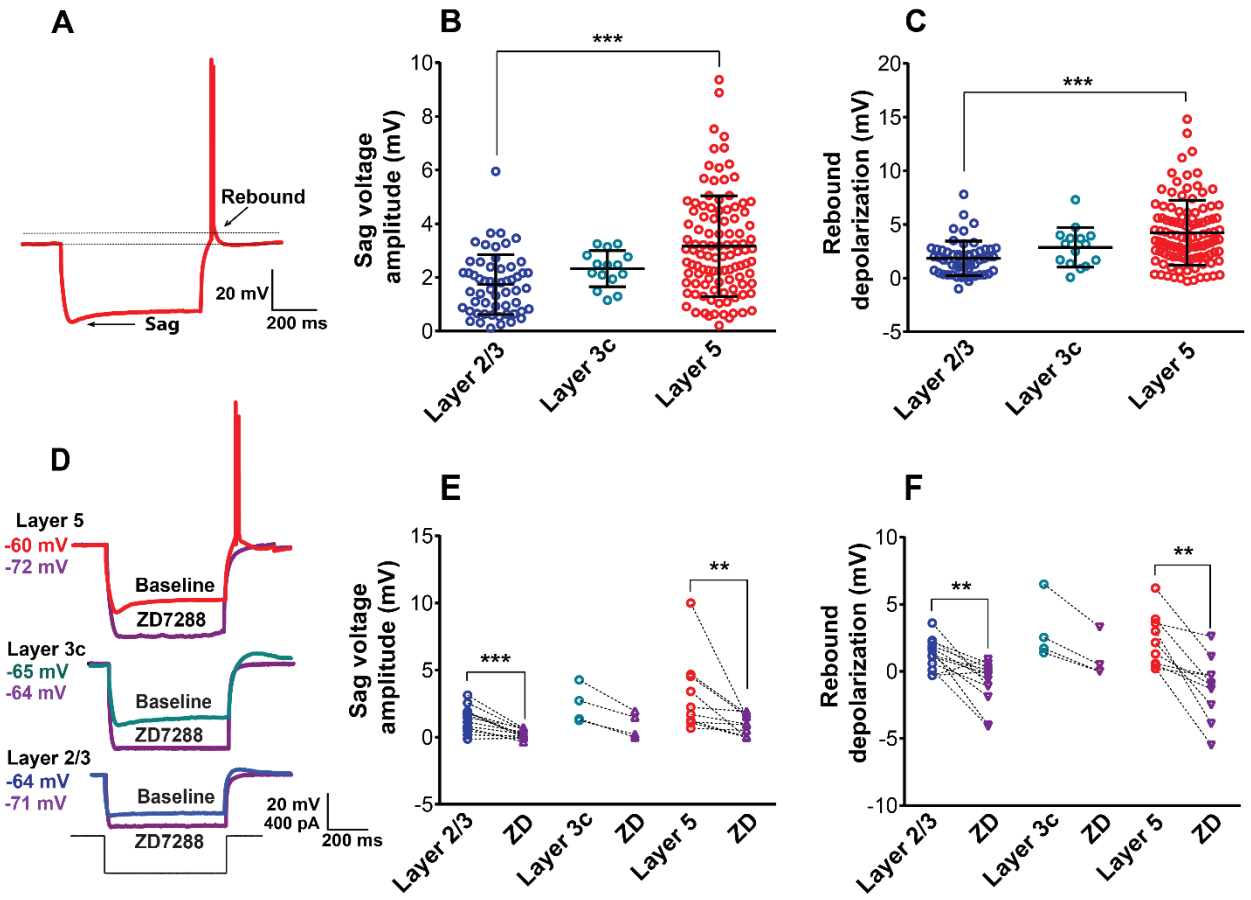

364 ***Figure 2. I_h related membrane properties are more profound in L5 pyramidal cells compared to L2/3 and***
365 ***L3c. (A)*** Example voltage sweep from a representative L5 pyramidal cell during injection of -400 pA
366 hyperpolarizing current step. Arrows indicate sag voltage and rebound depolarization and post-
367 hyperpolarization rebound spiking. **(B, C)** Sag voltage amplitude (B) and rebound depolarization amplitude
368 (C) among sampled L2/3, L3c, and L5 pyramidal cells in response to injection of hyperpolarizing current.
369 Lines and error bars denote mean and SD and asterisks indicate significance of group comparison. ***
370 indicates $p < 0.001$, Wilcoxon non-parametric test. **(D)** Example of voltage sweeps at baseline (red, green,
371 and blue) and after (purple) bath application of the I_h blocker ZD7288 (10 µM) following injection of -400
372 pA. **(E, F)** Bath application of ZD7288 diminished sag voltage amplitude (E) and rebound depolarization
373 amplitude (F) in all layers. ** indicates $p < 0.01$, Wilcoxon non-parametric test.

374

375 *3.3. Suprathreshold active membrane properties of pyramidal cells in layers 2/3 and 5*
376

377 Active membrane property differences between layers, was characterized by examining the firing
378 patterns of L2/3, L3c and L5 human pyramidal cells (n=55, n=15, n=104 neurons respectively) using a series
379 of depolarizing current pulses (0-400 pA, 600ms) with examples shown in Figure 3A, B and C. L5 neurons
380 had a significantly larger action potential than L2/3 neurons (L2/3: 81.9 ± 13.2 mV, L3c: 88.3 ± 7.5 mV, L5:
381 88.7 ± 18.2 mV, p=0.02; Figure 3D). In addition, the action potential half-width was similar in L5 compared
382 to L2/3 (L2/3: 1.8 ± 0.6 ms, L5: 1.8 ± 0.7 ms). However, the half-width of the action potential was

significantly longer in L3c pyramidal cells compared to L2/3 and L5 pyramidal cells (L3c: 2.2 ± 0.6 ms, p=0.02; Figure 3F).

The frequency-current relationships (f-I curve) showed greater f-I slopes for L5 relative to L2/3 and L3c neurons (Figure 3G; at 300 pA, L2/3: 16.3 ± 12.2 Hz, L3c: 11.0 ± 12.2 Hz, L5: 21.8 ± 13.1 Hz, p=0.0026 between L2/3 and L5 neurons, and p = 0.0011 between L5 and L3c neurons). The current needed to elicit an action potential was significantly lower in L5 neurons compared to L2/3 (L2/3: 162.1 ± 81.9 pA, L3c: 153.5 ± 66.6 pA, L5: 121.1 ± 85.2 pA, p=0.002 between L2/3 and L5; Figure 3H). We also note that these distributions were especially broad, in particular for L5 pyramidal cells, mirroring the large range in input resistances and diverse morphologies of these neurons (Figure 1). L5 neurons showed significantly less spike frequency adaptation relative to L2/3 and L3c neurons (L2/3: 0.16 ± 0.16, L3c: 0.25 ± 0.16, L5: 0.11 ± 0.13, p=0.01 between L5 and L2/3, p=0.0009 between L5 and L3c; Figures 3I). Lastly, we identified a small number of bursting neurons (defined as those with instantaneous frequencies at rheobase > 75 Hz) in our dataset (e.g., the L5 cell illustrated in Figure 3C and further examples in Figure S3). Specifically, we found 14% of our recorded L2/3 pyramidal cells and 9.5% of L5 pyramidal cells showing bursting activity. The overall low number of bursting neurons in both superficial and deeper cortical layers of human neocortex are consistent with previous report of infrequent bursting in human neocortex [3].

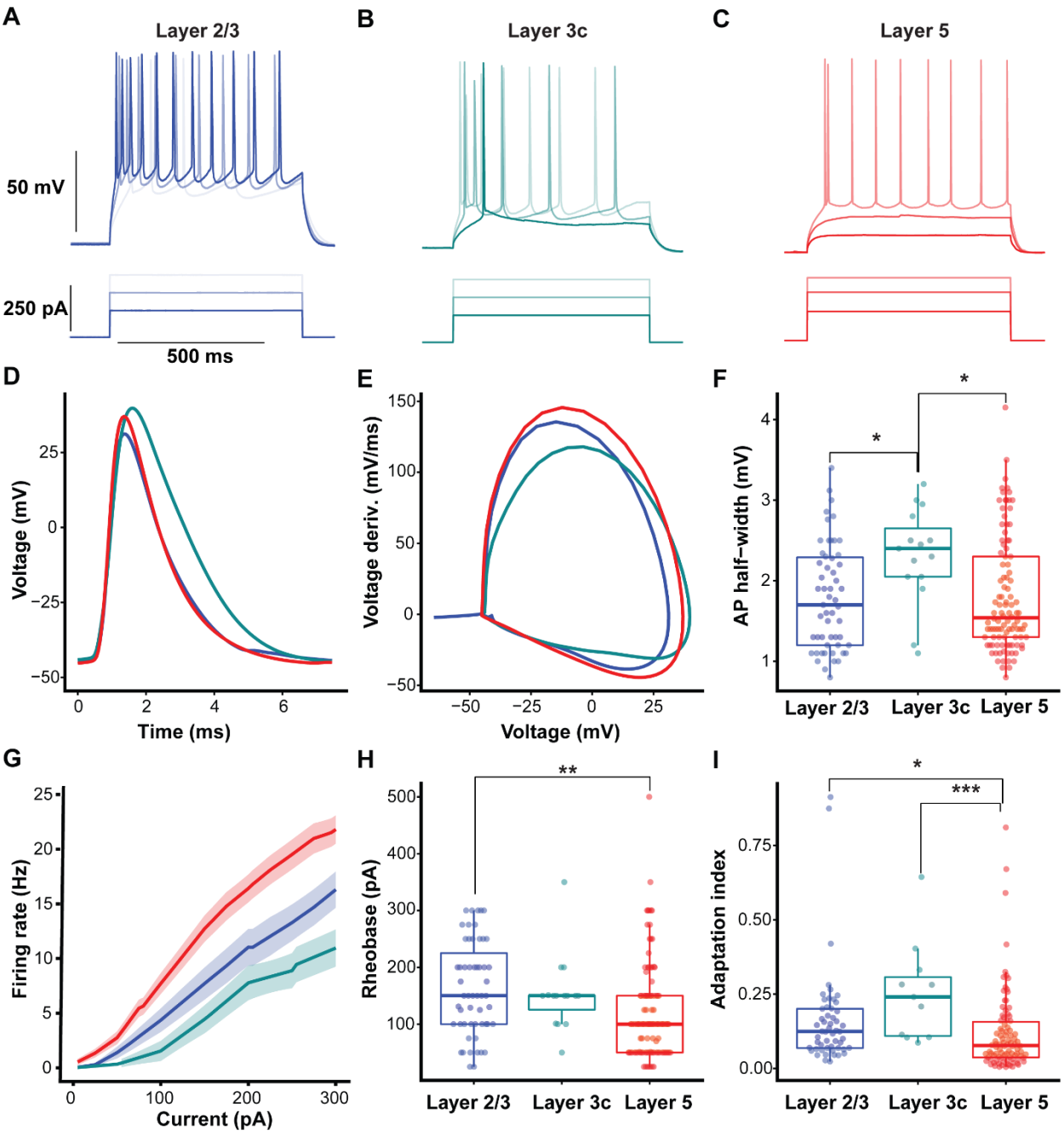

411

412 **Figure 3. L5 pyramidal cells display higher frequency firing rate and less adaptation than L2/3 and**
413 **L3c neurons. (A, B, C)** Example L2/3, L3c and L5 pyramidal cell voltage responses following depolarizing
414 current injections (150 pA, 250 pA and 300 pA, 600 ms). **(D, E)** Action potential waveform (D) and action
415 potential phase plot (E) averaged over recorded pyramidal cells in each layer. **(F)** L5 pyramidal cells had a
416 smaller action potential half-width compared to L2/3 and L3c neurons which was not significant in
417 comparison with L2/3 neurons. Half-width of action potential was higher significantly in L3c pyramidal cells
418 compared with L2/3 and L5 neurons. **(G)** Current versus firing rate relationships (FI curves), averaged over
419 pyramidal cells recorded in each layer. Shaded bands indicate SEM. **(H)** L5 pyramidal cells needed less
420 depolarizing current to display first action potential compared to L2/3 and L3c neurons. **(I)** L5 pyramidal
421 cells show less spike frequency adaption, quantified using the adaptation index measure, in comparison

with L2/3 and L3c. *** indicates $p < 0.001$, ** indicates $p < 0.01$, * indicates $p < 0.05$, Wilcoxon non-parametric test.

3.4. Subthreshold and suprathreshold resonance in human pyramidal cells across cortical layers

Resonance is a common approach to characterize the frequency preferences of neurons and represents the net result of the interaction between passive and active properties [42]. Moreover, I_h is an active current shown to contribute to low pass filtering properties of pyramidal cells due to its slow activation and deactivation [22]. Indeed, human pyramidal cells, and in particular those in deeper part of L3 as well as thick-tufted neurons in L5, can exhibit low frequency subthreshold resonance [3,4]. These findings in human neurons are consistent with studies in rodent cortex that describe the correlation between a large sag voltage and low frequency resonance [33].

We examined subthreshold resonance in our recorded L2/3, L3c and L5 pyramidal cells using a 20s-long frequency-modulated (or ZAP) current stimulus delivered at the resting potential [22]. Our analysis revealed clear examples of resonant pyramidal cells in each of the 3 major layers we profiled (Figure 4A and B). Our analyses identified a number of neurons that displayed a non-zero peak in their resonant frequency (fR; 27% of L2/3 neurons; 47% of L3c neurons; and 40% of L5 neurons) but considerably few neurons with resonant frequencies greater than 2Hz (Figure C). We found qualitatively similar results when repeating the ZAP current injection while holding neurons near -80 mV in a subset of neurons (data not shown). We found there was a slight trend for a decrease in the 3 dB cutoff frequency in L5 relative to L2/3 neurons ($p = 0.05$, Figure 4D). These results are generally consistent with recent evidence for greater subthreshold resonance in the deeper part of the supragranular layers of the human neocortex relative to more superficial neurons [4]. However, based on prior work [3] we were surprised that subthreshold resonance, was not more prevalent in these data (see Discussion).

We further compared the frequency response characteristics of L2/3 and L5 pyramidal cells in response to suprathreshold ZAP current injections, with example traces shown in (Figure 4E). We found that L5 neurons spike with greater fidelity to higher frequency stimuli (12-18 Hz) relative to L2/3. We did not observe a difference in frequency tracking at other frequency ranges (Figure 4F), including frequencies at delta or theta (1-8 Hz).

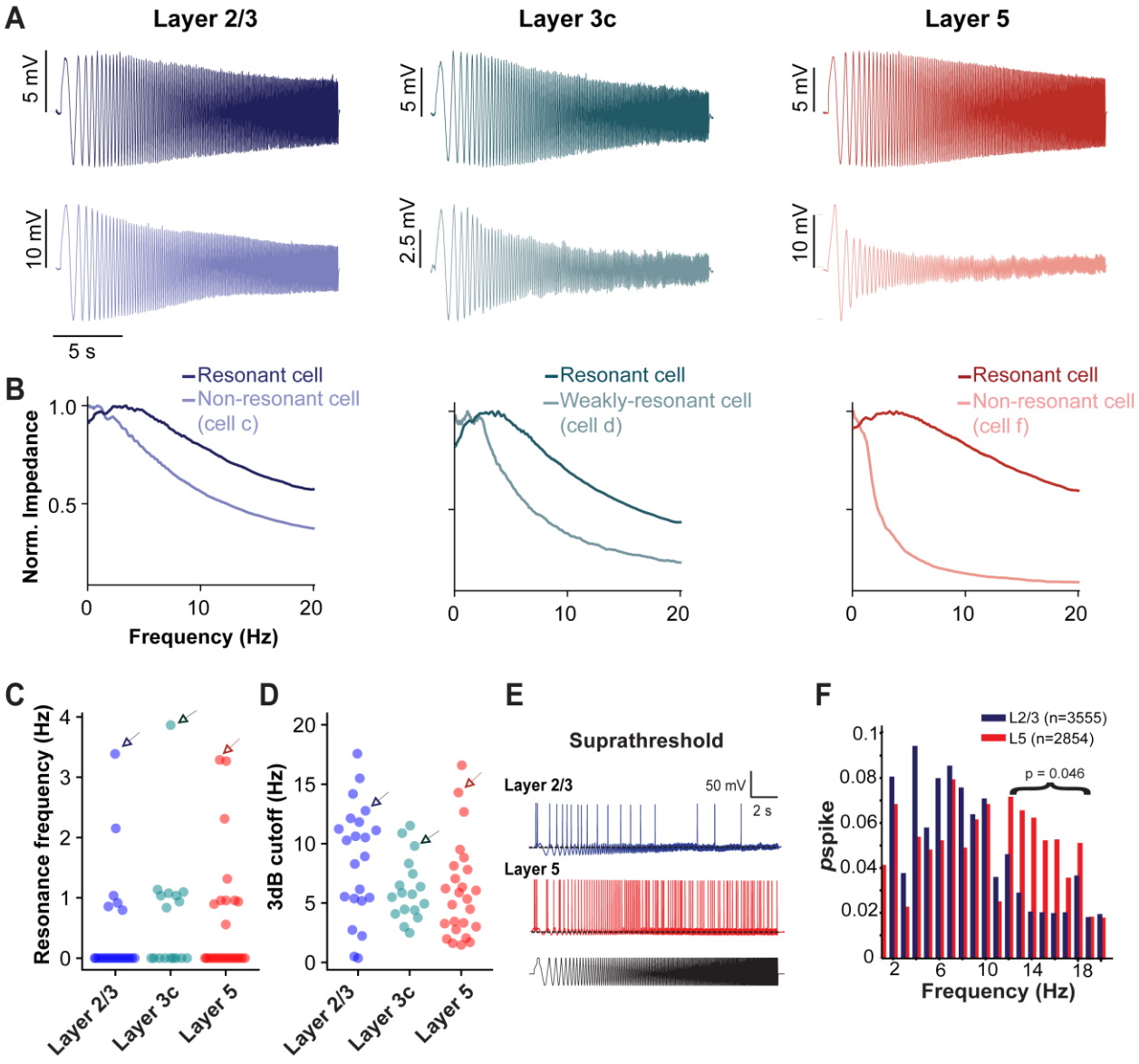

Figure 4. Subthreshold and suprathreshold resonance properties of L2/3, L3c and L5 pyramidal cells. **(A)** Example voltage responses following injection of subthreshold frequency-modulated (ZAP) current delivered at resting potential in L2/3, L3c and L5 pyramidal cells. Voltage traces are averaged across 5 repeated trials. Top voltage trace indicates response for an example cell displaying subthreshold resonance and bottom trace indicates response for a non-resonant cell. Cell labels are provided below in B and naming of cells corresponds to example cell morphologies shown in Figure 1. **(B)** Normalized impedance profiles for the voltage traces shown in A, with impedances normalized to a maximum value of one. **(C, D)** Resonance frequencies (C) and 3dB cutoff frequencies (D) indicate that there are relatively few strongly resonant pyramidal cells in our dataset. Arrows in C and D correspond to resonant cells highlighted in A and B. A subset of recorded neurons were recorded in the presence of synaptic blockers. **(E)** Example voltage responses following injection of suprathreshold ZAP current. **(F)** Spike response probability in response to suprathreshold current injection show that L2/3 and L5 pyramidal cells track theta frequencies

with high fidelity. The distributions were not significantly different (KS*p* = 0.53). Above 12Hz spike probabilities differed significantly between L2/3 and L5.

3.5. Putative interneurons recorded in L5 show greater amounts of sag and subthreshold resonance relative to L2/3

Our data set also included a number of putative GABAergic interneurons (examples in Figure 5A; L2/3: n= 10, L5: n= 14). We were able to distinguish putative interneurons from pyramidal cells by their action potential characteristics (Figure 5B, C), large maximal firing rates, and typically large spike after-hyperpolarization amplitudes (see Fig S4 for morphological corroboration for one putative interneuron from our dataset). In the context of previous results [4] and our current ones, we were curious if the general organizing principle of increased sag with increased depth from pia held for this class of neurons too.

Indeed, the set of putative interneurons in L5 had significantly larger sag voltage amplitudes compared to putative interneurons in L2/3 (L2/3: 1.2 ± 1.1 mV, L5: 4.5± 3.7 mV, p=0.001; Figure 5D). Moreover, L5 putative interneurons had significantly larger rebound depolarization amplitudes relative to L2/3 putative interneurons (L2/3: 1.7 ± 2.2 mV, L5: 5.2± 3.2 mV, p=0.003; Figure 5E). These results mirror our overall findings in the analogous pyramidal cells from these layers. Moreover, while there was a relatively small number of interneurons that were characterized with ZAP current injection (examples in Figure 5F-G), we noticed a comparatively large fraction of L5 putative interneurons that displayed a non-zero peak in their resonant frequency (3 of 6 neurons) compared to L2/3 (1 of 3 neurons) (Figure 5H). Although a small number of neurons and thus requiring corroboration, these data are consistent with prior reports of strong subthreshold resonance activity in human cortical GABAergic interneurons [5] and in rodent hippocampal interneurons [43]. These results suggest that depth from pia appears is certainly a general organizing principle for sag current in the cortex for both excitatory and inhibitory neurons.

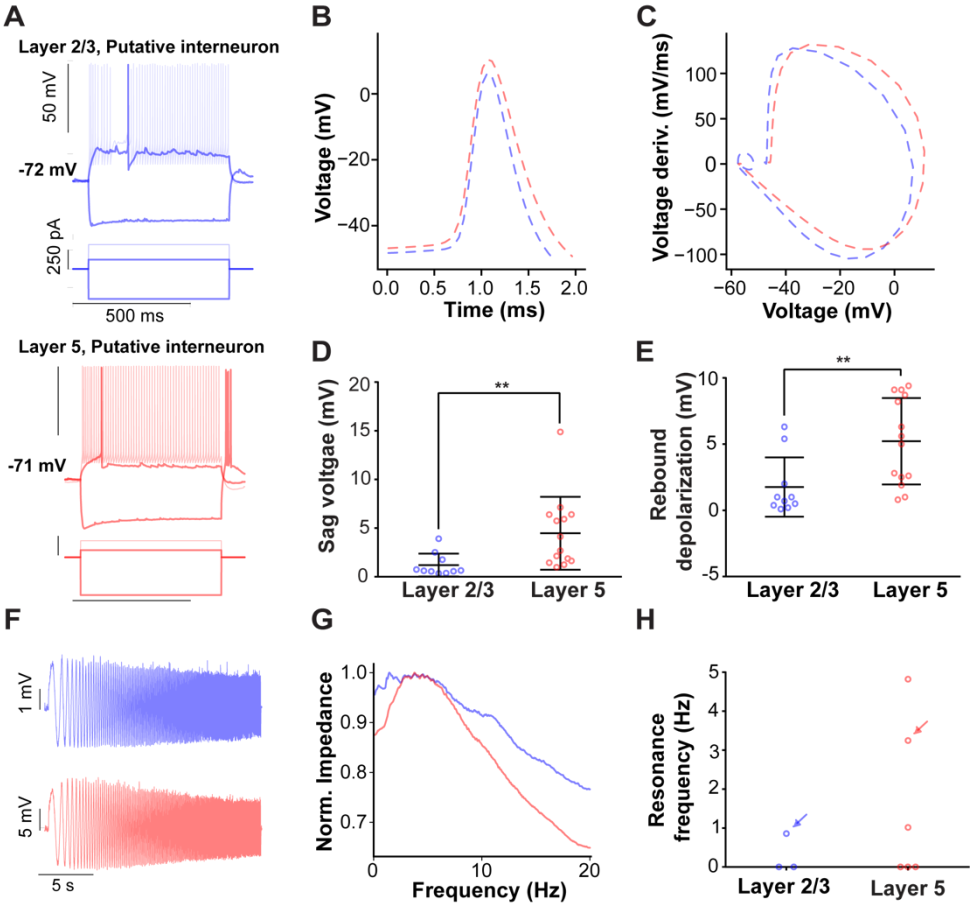

Figure 5. Electrophysiological and subthreshold resonance properties of putative interneurons recorded in L2/3 and L5. (A) Example voltage responses and current steps for an example putative interneuron from a L2/3 (top) and L5 (bottom). **(B, C)** Action potential waveform (B) and action potential phase plot (C) averaged over recorded putative interneurons in L2/3 (blue) and L5 (red). **(D, E)** Sag amplitude (D) and post-hyperpolarization rebound depolarization amplitude (E) reveals greater amounts of sag and rebound depolarization amplitude in L 5 putative interneurons compared to L2/3. ** indicates $p < 0.01$, Wilcoxon non-parametric test. **(F, G)** Example subthreshold voltage responses (F) and normalized impedance (G) following ZAP current injection for example neurons shown in A. **(H)** Subthreshold resonance frequencies show a trend for more subthreshold resonance in L5. Arrows indicate neurons highlighted in F.

3.6. Considerable heterogeneity and overlap in electrophysiological features among pyramidal cells sampled across different layers of the human neocortex

Given the large degree of variability among intrinsic electrophysiological features in the pyramidal cells in our study, we next sought to identify gradients or sub-clusters among these neurons. For example, in rodent neocortex, there is strong convergent evidence that pyramidal cells from L5 are split into two major subclasses, with neurons from L5a more likely to be regular spiking, intra-telencephalic projecting (IT). Such neurons show slender tufted dendritic morphologies compared to pyramidal cells in L5b, which are more likely to be bursting, extra-telencephalic (ET), and show thick-tufted dendritic morphologies [44,45]. While in human neocortex there is some recent evidence for this dichotomy based on transcriptomics data,

with the implication that there are likely far fewer ET neurons than IT neurons in L5 relative to the rodent setting [46], to our knowledge this has yet to be corroborated at the electrophysiological and morphological levels.

We addressed this question using dimensionality reduction techniques to arrange our neurons by similarity in multi-variate sets of electrophysiological features (L2/3: n= 56, L3c: n = 14, L5: n= 103 neurons). We specifically used UMAP [34], using 14 subthreshold and suprathreshold electrophysiological features that were consistently calculated in the majority of pyramidal cells within our dataset (see Methods). We found some evidence for gradients and/or subclusters among the sampled neurons based on the input electrophysiological features (Figure 6A). Upon further inspection, we found that a single major factor, related to cell input resistance and rheobase current, appeared to qualitatively define the major gradient underlying the differences in neurons highlighted by this analysis (Figure 6B). We were able to corroborate aspects of this unbiased analysis through inspection of pyramidal cell morphologies (where available), with neurons at one extreme of the gradient having the largest input resistances and the most simple morphologies (e.g., cell a and cell f from Figure 1). Similarly, neurons with morphologies on the other side of the gradient tended to have lower input resistances and more complex morphologies, such as the putative thick-tufted cell (cell g) shown in Figure 1. This analysis also revealed that neurons throughout the gradient tend to show bursting behavior (Figure 6C) and that neurons with intermediate input resistances (such as those sampled from L3c) are more likely to display subthreshold resonance (Figure 6D).

The other major finding of this analysis is that neurons from each of the layers we sampled were often inter-mixed in the low-dimensional space, with neurons from L2/3 often displaying very similar electrophysiological profiles to those sampled in L5. The pyramidal cells sampled from L3c were one exception, however, as these were present primarily at a single position in the low-dimensional space, along with other neurons of intermediate input resistance. As we did not see strong evidence for a subtype of L5 neurons that were electrophysiologically distinct from those in L2/3 and other L5 neurons, we conclude that either we do not have L5 ET neurons present in our dataset or that we are unable to distinguish them from IT neurons using these electrophysiological features alone (see Discussion).

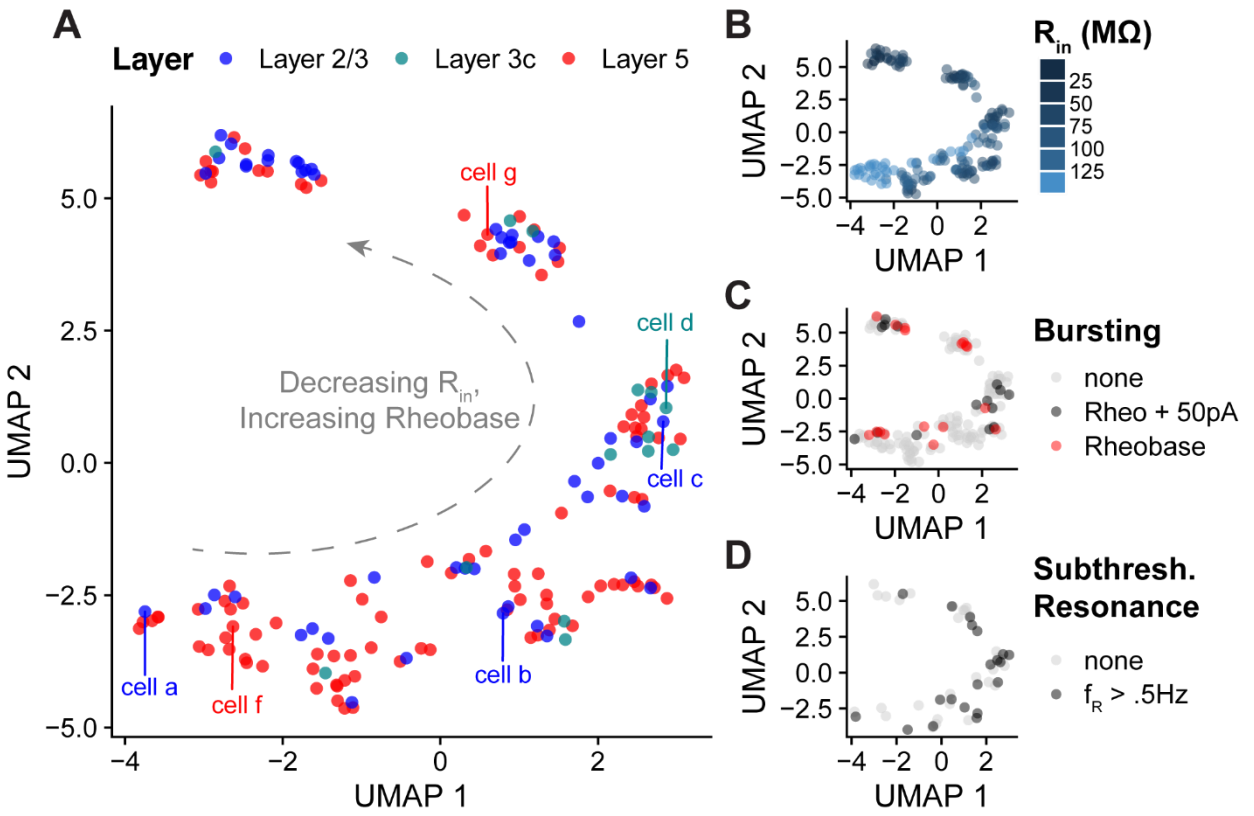

Figure 6. Dimensionality reduction reveals considerable intrinsic electrophysiological similarity and overlap between pyramidal cells recorded in different layers. (A) Dimensionality reduction analysis performed on multivariate sets of electrophysiological features using Uniform Manifold Approximation (UMAP). Neurons are arranged by similarity in intrinsic electrophysiological features (see methods for list of features used in analysis). Cell labels correspond to neurons whose morphologies are highlighted in **Figure 1**. (**B-D**) Same as A, but neurons are colored by input resistance (B), bursting behavior (C), or subthreshold resonance (D). Bursting behavior in C is broken down by neurons that show no bursting, neurons that burst at rheobase current plus 50 pA, or neurons that burst at rheobase. Bursting is defined where the instantaneous firing rate is greater than 75 Hz.

3.7. Assessment of frequency-dependent gain reveals greater preference for delta and theta frequencies among L5 relative to L2/3 pyramidal cells

The frequency and phase preference of spike generation will determine a neurons ability to participate in the amplification/generation of oscillations [21] and as a "synchrony filter" [47]. To quantify this property, we characterized the frequency dependent suprathreshold spiking properties of L2/3 and L5 pyramidal cells, in a subset of neurons (n=8 neurons each for L5 and L2/3) from an additional set of patients (n=5). We stimulated neurons with multiple trials of a frozen filtered white noise current stimulus. We used this stimulus to compute the frequency dependent gain [*G(f)*] and the mean phase shift of the spike response (Figure 7A) [35]. The frequency dependent gain, *G(f)*, quantifies the phase preference of neuronal spiking as function of frequency [48]; intuitively, neurons with a high gain at a specific frequency are more likely to fire in phase with a sine-wave at that frequency than at other frequencies.

We found both that L2/3 and L5 neurons displayed peaks in *G(f)* within the delta and theta frequency ranges (Figure 7B). Both peaks were more pronounced in L5 pyramidal cells compared to L2/3 ($p<0.05$). Additionally, above 10Hz, we found that L5 pyramidal cells displayed greater frequency

574 dependent gain than L2/3 neurons, consistent with the suprathreshold ZAP results. The greater excitability
575 and fidelity of L5 neurons was also evident in their phase curves and spike triggered averages (STAs) (Figure
576 7C, D). L2/3 neurons demonstrated a greater lag in firing than L5 neurons, and their STA were of larger
577 amplitude with steeper slopes. This suggests that L2/3 neurons require larger inputs to trigger spikes, and
578 when they do spike, they will lag behind L5 pyramidal cells if inputs are coincident.

579 We more precisely explored the potential contribution of I_h to low frequency rhythms via its
580 influence on *G(f)*. For both L2/3 (n=3, Figure 7E) and L5 pyramidal cells (n=3, Figure 7F), ZD7288 (an I_h
581 blocker) was applied to compare *G(f)* before and after abolishing the I_h. We found that blocking I_h
582 predominantly abolished the delta peak in L5 neurons, and to a lesser extent the theta peak in both L2/3
583 and L5 neurons. These data indicate that L5 pyramidal cells are better at tracking both delta and theta
584 frequency inputs than superficial layer neurons (although L3c neurons were not tested in this way), and
585 that the larger the I_h in L5 pyramidal cells imbues them with increased responsiveness to delta frequency
586 inputs.

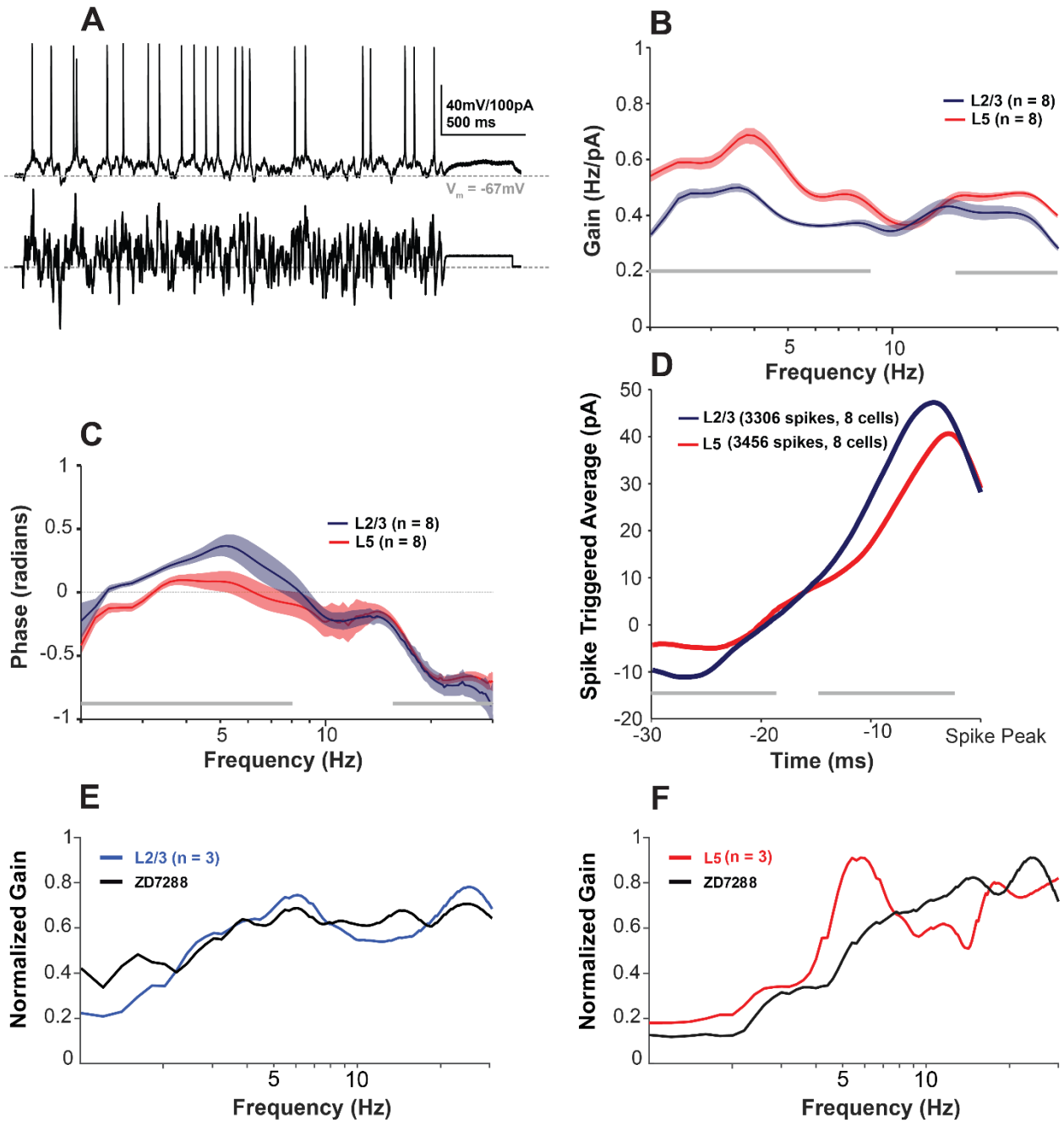

Figure 7: Human L5 neurons display greater gain at delta and theta frequencies than L2/3 pyramidal cells. (A) Example of V_m response to 2.5s of frozen filtered noise current injection stimulus for a L5 pyramidal cell. **(B)** Frequency dependent gain profile of L2/3 and L5 pyramidal cells over a wide range of frequencies. Frequency dependent gain, G(f), was calculated with frequency-dependent windowing (see Materials and Methods). Both layers show two peaks around 2.5-10 Hz, and 12-16 Hz which are more pronounced in L5 pyramidal cells compared to L2/3. Gray horizontal bars represent significant differences between groups. **(C)** Phase shift of spiking relative to input stimulus. L2/3 pyramidal cells show positive phase in their mean phase shift profile which represents a lag in L2/3 pyramidal cells compared to L5 pyramidal cells. **(D)** Mean spike triggered average (STAs) for L5 and L2/3 neurons. Difference in STAs indicate L5 neurons require less current and instantaneous rate of current increase to initiate a spike

(greater excitability). (**E, F)** Frequency dependent gain profile of L2/3 (E) and L5 (F) pyramidal cells before and after I_h blocker (ZD7288 10 μM). ZD7288 abolished the low frequency peaks in L5 neurons with little change in frequency dependent gain in L2/3 neurons.

3.8. Replication of major findings in an additional cohort of patients and identification of a provisional relationship between sag and patient age

To close, we wondered if the major findings of this work would generalize if tested in an additional group of human neurosurgical patients. To this end, we utilized a publicly-accessible dataset of 272 pyramidal cells sampled from L2, L3, and L5 from an additional cohort of 39 human surgical patients characterized by the Allen Institute for Brain Sciences (http://celltypes.brain-map.org/). We note that while the overall experimental design of the Allen Institute's dataset is similar to ours, there are some key methodological differences, such as the composition of solutions used for slice preparation and recording (see Methods). In addition, because of differences in the amplitudes of hyperpolarizing current steps used to assess sag, we chose to cross-compare these datasets using the dimensionless sag ratio measure, defined as the ratio between the sag amplitude and the hyperpolarization-evoked peak voltage deflection from the resting potential. We note that sag ratio is positively correlated with sag amplitudes (Figure S5, r = 0.68). One final caveat with the Allen Institute dataset is that L5 pyramidal cells have not been annotated for the ET or IT subtype, similar to our own dataset.

We were able to use the Allen Institute cohort to replicate our primary finding that L5 pyramidal cells have larger sag ratios than pyramidal cells in L2 and L3 (Fig S6; L2: 0.51 ± 0.045; L3: 0.125 ± 0.067; L5: 0.149 ± 0.072; $p = 2.21 \times 10^{-6}$ between L2 and L3, p = 0.012 between L3 and L5). Similarly, these data are consistent with our finding that input resistances in L5 pyramidal cells are not smaller than those sampled in human L2 and L3 (Figure S7A; L2: 105 ± 49.9; L3: 89.7 ± 57.7; L5: 170 ± 74.7) and that trend holds even in neurons where the primary dendrites are not visibly truncated (Figure S7B).

Lastly, we investigated if some of the cell-to-cell variability in sag could be in part explained by patient-level demographic features, such as patient age at time of surgery. To address this question, we cross-referenced our recordings with basic demographic information from patient medical records where available, yielding a total of 137 pyramidal cells sampled from L2/3 and L5 in 42 patients. In the L5 pyramidal cells sampled in our dataset (the Krembil Institute cohort), we found that there was a trend for neurons recorded from older patients tended to have larger sag ratios than those from younger patients (Figure 8A, r = 0.21, p = 0.10, based on a mixed-effects statistical model with subject ID as a random effect, see Methods). When we investigated analogous L5 pyramidal cells from the Allen Institute cohort, we found a consistent relationship between patient age and sag ratios that was statistically significant (Figure 8B, r = 0.30, p = 0.014). Assessing this relationship in L2/3 pyramidal cells, we found a similar overall relationship in data from the Krembil Institute cohort (Figure 8C, r = 0.36, p = 0.022). While we found a relationship in the same direction in the Allen Institute cohort for L2/3 neurons, we note that the relationship was not statistically significant (Figure 8D, r = 0.11, p = 0.30), possibly due to differences in the relative compositions of L2 versus L3 pyramidal cells sampled in each cohort and the confound that differences in somatic depth among L3 pyramidal cells also influence the amount of sag observed [4]. Given the challenges in comparing neurons recorded across patients (e.g., this analysis likely pools neurons sampled from different cell types, like ET vs IT), we note that these correlations should be seen as provisional. Moreover, it is possible these correlations may not be replicated in other cohorts; for example, in a recent study of L5 human pyramidal cells [3], no correlation between age and dendritic sag magnitudes were observed.

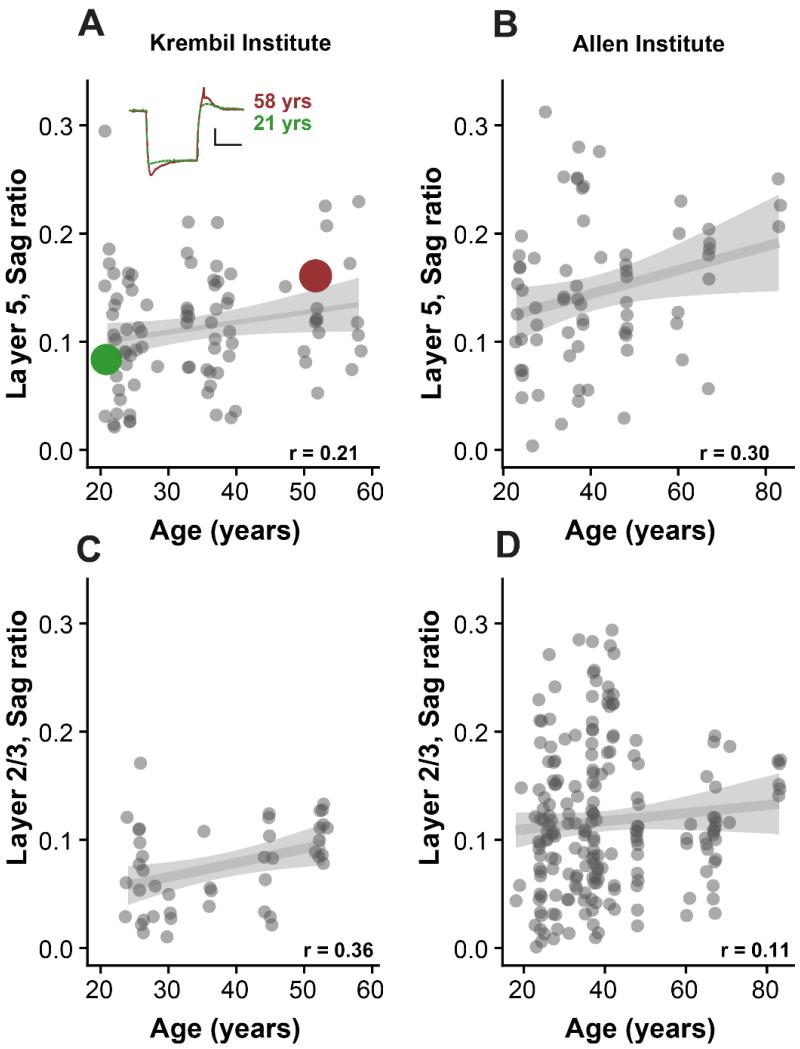

Figure 8: Correlation between pyramidal cell sag ratios and patient age. (A) L5 pyramidal cell sag ratio values as a function of patient age for neurons sampled from the Krembil Institute cohort. Each grey dot reflects one cell and multiple neurons are typically sampled per patient. Inset shows example voltage trace data for two representative neurons. Grey line indicates linear fit. Inset correlation values based on a linear mixed effects model. **(B)** Same as A, but for data from the Allen cohort. **(C-D)** Same as A and B, but for L2/3 pyramidal cells sampled from the Krembil Institute cohort (C) or the Allen Institute cohort (D).

4. Discussion

Guided by our previous work implicating deep layer human pyramidal cells in driving coherent low frequency oscillations in human neocortex, we sought to characterize the electrophysiological differences between deep and superficial human pyramidal cells. We summarize five major findings from this work:

First, considering each broad cortical layer as a group, we found that there is a gradient of increased excitability from superficial to deeper layer pyramidal cells, with L2/3 pyramidal cells demonstrating more hyperpolarized resting potentials, lower input resistances and larger rheobase required for spike

generation, enhanced spike frequency adaptation, and steeper and larger amplitude spike triggered averages. Along most of these features, the neurons sampled from L3c were often at an intermediate point between L2/3 and L5.

Second, we found enhanced sag and I_h-related features in L5 neurons relative to L2/3 neurons, again with L3c neurons intermediate between these groups. I_h appeared to be one of the major contributors to the prominent rebound depolarization and rebound spiking in human L5 neurons, as ZD7288 significantly reduced both. I_h also contributes to enhanced frequency-dependent gain at delta and theta frequencies and is more prominent in L5 relative to L2/3 pyramidal cells, which we could abolish using ZD7288. Intriguingly, we found anecdotal evidence that I_h appears more prominent in L5 relative to L2/3 putative GABAergic interneurons, and that this might contribute to enhanced resonant activity in these neurons.

Third, we found a number of pyramidal cells displaying subthreshold resonance, with the greatest fraction of resonant neurons observed in L3c. These findings support previous reports of strong subthreshold resonance in pyramidal cells, in particular in the deeper parts of L3 and in larger, thick-tufted neurons in L5 [3,4].

Fourth, we found a great degree of electrophysiological heterogeneity among pyramidal cells sampled within each cortical layer, and that this heterogeneity in part reflects coordinated complexity in dendritic morphologies. Mirroring recent reports that there is great deal of variability in morpho-electric and transcriptomic subtypes of L2 and L3 pyramidal cells [4,41], we found that there is a similar (and possibly even greater) amount of electrophysiological variability among human L5 pyramidal cells. One source of the variability, in L5 in particular, could be the known dichotomy between extra-telencephalic (ET) and intra-telencephalic (IT) projecting neurons, as has been extensively described in rodents [44,45]. In contrast to a recent report from human L5 that specifically targeted large thick-tufted neurons [3], the majority of the L5 neurons sampled here show relatively high input resistances (>90 MΩ), and we hypothesize are thus likely to be thin-tufted, IT pyramidal cells. While our sampling of neurons is not without its own biases, our sampling of L5 neurons is consistent with recent transcriptomic evidence suggesting that the vast majority of excitatory neurons in human L5 are likely to be IT, in stark contrast to the rodent setting [46]. However, an additional explanation for the variability could be within cell type heterogeneity, which is increasingly recognized as an important and biologically meaningful aspect of neural circuits [49].

Fifth, leveraging the large sample of patients in our study, we found suggestive evidence that pyramidal cells from recorded older patients tended to show greater amounts of sag relative to pyramidal cells recorded in younger patients. By replicating this finding using publicly accessible data collected by the Allen Institute from a second cohort of human patients, we were able to gain additional confidence in the generalizability of this relationship.

4.1. Relationships between I_h and cortical rhythmogenesis in human pyramidal cells

Given our findings of greater I_h in L5 neurons, we were initially surprised that a larger number of neurons did not demonstrate a peak in subthreshold resonance. For example, a previous report by Kalmbach, B et. al (2018) suggested that I_h contributes to prominent subthreshold resonance in deep L3 human pyramidal cells [4]. Similarly, somatic subthreshold resonance has also been reported in human L5 thick-tufted neurons [3]. In addition, previous work in rodents has shown that L5 pyramidal cells are

associated with the genesis of subthreshold frequency resonance[8,50-52]. It has been proposed that this band pass filtering is mediated by interactions between I_h [50], persistent Na^+ current (I_{NaP}), I_{IR} (instantaneously activating, inwardly rectifying K^+ current) [51], M-current and passive properties of L5 pyramidal cells [52]. However, previous investigations of subthreshold resonance have shown that I_h alone is not sufficient to account for the high pass filtering that gives rise to a resonant peak; in fact, it is likely a more complex interaction of the presence of I_h, along with the kinetics of this channel, the neuron's morphology, and its passive properties that dictates whether a cell will demonstrate a low frequency resonant peak.

Hippocampal oriens-lacunosum molecular (OLM) interneurons, for example, exhibit a large characteristic sag, indicative of the presence of I_h, without displaying subthreshold resonance [43]. When comparing OLM neurons to CA1 pyramidal cells as well as oriens-radiatum (OR) interneurons that have I_h and resonance, Zemankovics, R et. al. (2010) identified minimal difference in the I_h conductance between the three neuron types. Instead, a significant difference in the voltage dependence of the h-channel kinetics was identified between the two interneuron types and the pyramidal cells, but not between the OLM and OR interneurons, indicating that these kinetics might account for some, but not all, of the tendency of these neurons to resonate. Zemankovics, R et. al. (2010) further suggest that differences in passive properties between the OLM and OR neurons underlie the different resonance characteristics in these interneurons [43]. The work of Hu, H et. al. (2002) identified multiple mechanisms by which resonance can occur, including one mediated by the M-current [22]. Additionally, in inferior olivary neurons it is the low threshold calcium current that underlies these neurons' low frequency resonance [53]. These results imply that I_h is neither necessary nor sufficient in the generation of low frequency resonance. Taken together, they also suggest a more complicated picture of the relationship between the presence of I_h and the capacity for a neuron to exhibit subthreshold resonance, a situation wanting for computational modeling and in silico explorations to help fully describe this aspect of human L5 physiology [15].

Recently a putative 'dynamic circuit motif' (DCM) [21] has been proposed to underlie the interlaminar nested delta-theta oscillations observed in rodents. This DCM posits intrinsically-bursting (IB), ET neurons in L5 neurons as a central actor in generating deep layer activity that drives superficial theta oscillations [54]. Although, the electrophysiological signature and experimental conditions studied in Carracedo, L et. al. (2013) were different that our studies in human cortical slices, it is instructive to relate our findings to what was observed in rat neocortex. Carracedo, L et. al. (2013) demonstrated that delta oscillations likely occur due to tonic drive to the dendrites of IB neurons in superficial layers. This tonic drive causes the IB neurons to discharge bursts at delta frequencies (~2Hz). IB neurons are unique in that, in addition to their subcortical targets, they primarily synapse locally within deep layers on L5 regular-spiking (RS) IT neurons, unlike L5 RS neurons that project axons both locally and to L2/3 [45,55,56] The RS neurons are thus driven by periodic barrages at delta frequencies and discharge doublets with each IB burst, thus generating "theta" frequency output at double the L5 delta frequency that is transmitted to superficial layers. The sinks generated in the superficial layers thus occur at theta frequency, driving local excitability in L2/3 with the resultant increase in excitatory drive to L5 IB dendrites and the cycle begins.

Our results demonstrating 4 and 8Hz peaks in *G(f)* for L5 RS neurons interpreted in the context of the above findings by Carracedo, L, et al (2013) provides a possible mechanism for the theta activity (~8Hz) that we observed in vitro, [57] and that is ubiquitously observed (~7Hz) in the human brain [18]. It is first important to note that the theta generated by RS neurons described by Carracedo, L et al (2013), arises from the doublet generated in response to each cycle of delta, and thus why theta (~4Hz) was twice the frequency of the observed delta (~2Hz). The double peak in *G(f)* for human L5 RS neurons implies that RS neurons are tuned to both 4Hz and 8Hz activity, and not surprisingly the 8Hz peak in *G(f)* is similar to the frequency at which interlaminar coherence was observed in human slices [10], and is twice the frequency of the low frequency peak in *G(f)*. Our ZD data further supports this relationship between human delta and

theta, where the delta peak in *G(f)* in this different subset of neurons was ~5.5Hz, and the "theta" peak was at ~11Hz. That blocking I_h completely abolished the delta peak, suggests that I_h tunes L5 RS neurons to track IB output, which then in turn generate theta (double the frequency of delta) output. Interpreted together our frequency dependent gain, and ZAP results show that I_h does not directly contribute to tuning cortical oscillations at theta (~8Hz), but rather facilitates the generation of theta by allowing RS neurons to track delta oscillations (see Figure S8 for schematic of this description).

An obvious difference between our previous human slice work [10] and that of Carracedo, L et al (2013) is that we observed robust deep layer theta (although theta was still more prominent in the superficial layers). One possible explanation is that the experimental conditions were dramatically different. Alternatively it has been shown in human cortical tissue, at least in L2/3, that single action potentials generate long lasting reverberant activity through rebound excitation that lasts an order of magnitude longer than in the rodent brain [7]. Thus, it is possible that such reverberant activity in L5 results in greater gain in local L5 cortical circuits that further amplifies theta activity through both synaptic activation, and the theta peak in *G(f)*. This conjecture is further supported by our observation that putative L5 interneurons demonstrate greater rebound than L2/3 neurons, and thus likely able to amplifying network activity within L5 potentially beyond what was observed in L2/3 [7]. Future experiments are needed to further explore if human cortical circuitry is arranged like that of the rodent, specifically as it relates to inter and intralaminar connectivity.

4.2. Limitations and caveats

It bears acknowledging that there are experimental limitations that might influence our observation of subthreshold resonance: the increased density of the HCN channel in the dendrites may result in this resonance being observed better in the dendrites compared to soma [3], and despite best practice controls there is the possibility that truncated dendrites might prevent resonance. Truncation of layer 5 pyramidal cell dendrites is a common and an unavoidable issue due to longer apical dendrite length in the human neocortex (2mm) [1,3]. However, there is strong evidence for increased dendritic compartmentalization in large human neurons with distal inputs attenuating strongly towards soma [3], and one would expect this effect to mitigate effects of dendritic truncation on subthreshold resonance.

An important caveat when interpreting these findings is that these data are exclusively collected from neurosurgical patients undergoing surgery for drug-resistant epilepsy or for resection of brain tumors. We note that we have been careful to only perform recordings from unaffected neocortical tissue distal from the epilepsy focus or tumor site. Nevertheless, it is unclear how these diseases (or their pharmacological treatment regimes) might contribute to compensatory changes at the level of cortical neuron physiology. However, by comparing our findings to the previous rich literature in rodents and to analogous human neuronal datasets collected by other groups, we can be more confident that the results presented here likely generalize to control human subjects.

4.3. Future implications of this work

This report reflects one of the largest studies of the electrophysiological diversity of human neocortical pyramidal cells to date. In particular, it contributes to our growing understanding of human L5 pyramidal cells [3] and helps put the unique characteristics of these neurons into context with the better understood superficial layer pyramidal cells.

Moving forward, it will be essential to reconcile these electrophysiological and morphological data with the emerging consensus of neocortical cell type diversity based on single-cell transcriptomics [3,4,46,58] and how these features contribute to the unique emergent properties of human cortical circuits. Furthermore, little is known about the connectivity within human cortical circuits: is human inter- and intra-

laminar connectivity similar to rodents, and how do cellular properties contribute to the signatures we observe in meso- and macroscopic recordings? Answers to these questions will require multi-scale inquires of human cortical micro-circuits and *in silico* experiments to understand the divergent properties of human circuits, with the tools for such inquiries only now becoming available.

Acknowledgements

We are immensely grateful to our neurosurgical patients and their families for consenting to the use of human brain tissue samples for research. We thank Dr. Gelareh Zadeh and Dr. Mark Bernstein for their assistance in obtaining brain tissue samples and Victoria Barkley and Marjan Rafiee for assistance compiling demographic and chart information. We thank Sara Mahallati and Xiao Luo for assistance in tissue preparation. We thank Brian Kalmbach for helpful conversations that informed our analysis of subthreshold resonance targeting of Layer 3c pyramidal cells. We thank Frances K Skinner, Etay Hay, Wesley Sacher, Xiao Luo, and Jasmine Bell for their critical comments on the manuscript. We acknowledge generous support from the CAMH, Krembil, and Kavli Foundations.

References

1 Mohan, H. *et al.* Dendritic and axonal architecture of individual pyramidal neurons across layers of adult human neocortex. *Cerebral Cortex* **25**, 4839-4853 (2015).

2 Eyal, G. *et al.* Unique membrane properties and enhanced signal processing in human neocortical neurons. *Elife* **5**, e16553 (2016).

3 Beaulieu-Laroche, L. *et al.* Enhanced dendritic compartmentalization in human cortical neurons. *Cell* **175**, 643-651. e614 (2018).

4 Kalmbach, B. E. *et al.* h-Channels Contribute to Divergent Intrinsic Membrane Properties of Supragranular Pyramidal Neurons in Human versus Mouse Cerebral Cortex. *Neuron* **100**, 1194-1208. e1195 (2018).

5 Boldog, E. *et al.* Transcriptomic and morphophysiological evidence for a specialized human cortical GABAergic cell type. *Nature neuroscience* **21**, 1185-1195 (2018).

6 Deitcher, Y. *et al.* Comprehensive morpho-electrotonic analysis shows 2 distinct classes of L2 and L3 pyramidal neurons in human temporal cortex. *Cerebral Cortex* **27**, 5398-5414 (2017).

7 Molnár, G. *et al.* Complex events initiated by individual spikes in the human cerebral cortex. *PLoS biology* **6**, e222 (2008).

8 Silva, L. R., Amitai, Y. & Connors, B. W. Intrinsic oscillations of neocortex generated by layer 5 pyramidal neurons. *Science* **251**, 432 (1991).

9 Silva, G. T. *et al.* Human synapses show a wide temporal window for spike-timing-dependent plasticity. *Frontiers in synaptic neuroscience* **2**, 12 (2010).

10 Florez, C. *et al.* In vitro recordings of human neocortical oscillations. *Cerebral cortex* **25**, 578-597 (2015).

11 Goriounova, N. A. *et al.* Large and fast human pyramidal neurons associate with intelligence. *Elife* **7**, e41714 (2018).

12 Skinner, F. K. Cellular-based modeling of oscillatory dynamics in brain networks. *Current opinion in neurobiology* **22**, 660-669 (2012).

13 Womelsdorf, T., Ardid, S., Everling, S. & Valiante, T. A. Burst firing synchronizes prefrontal and anterior cingulate cortex during attentional control. *Current Biology* **24**, 2613-2621 (2014).

14 Markram, H. *et al.* Reconstruction and simulation of neocortical microcircuitry. *Cell* **163**, 456-492 (2015).

15 Einevoll, G. T. *et al.* The Scientific Case for Brain Simulations. *Neuron* **102**, 735-744 (2019).

16 Ruzzo, E. K. & Geschwind, D. H. Schizophrenia genetics complements its mechanistic understanding. *Nature neuroscience* **19**, 523 (2016).

17 Vigo, D. V., Kestel, D., Pendakur, K., Thornicroft, G. & Atun, R. Disease burden and government spending on mental, neurological, and substance use disorders, and self-harm: cross-sectional, ecological study of health system response in the Americas. *The Lancet Public Health* **4**, e89-e96 (2019).

18 Groppe, D. M. *et al.* Dominant frequencies of resting human brain activity as measured by the electrocorticogram. *Neuroimage* **79**, 223-233 (2013).

19 McGinn, R. J. & Valiante, T. A. Phase–amplitude coupling and interlaminar synchrony are correlated in human neocortex. *Journal of Neuroscience* **34**, 15923-15930 (2014).

20 von Nicolai, C. *et al.* Corticostriatal coordination through coherent phase-amplitude coupling. *Journal of Neuroscience* **34**, 5938-5948 (2014).

21 Womelsdorf, T., Valiante, T. A., Sahin, N. T., Miller, K. J. & Tiesinga, P. Dynamic circuit motifs underlying rhythmic gain control, gating and integration. *Nature neuroscience* **17**, 1031 (2014).

22 Hu, H., Vervaeke, K. & Storm, J. F. Two forms of electrical resonance at theta frequencies, generated by M-current, h-current and persistent Na+ current in rat hippocampal pyramidal cells. *The Journal of physiology* **545**, 783-805 (2002).

23 Das, A. & Narayanan, R. Theta-frequency selectivity in the somatic spike-triggered average of rat hippocampal pyramidal neurons is dependent on HCN channels. *Journal of neurophysiology* **118**, 2251-2266 (2017).

24 Neuhoff, H., Neu, A., Liss, B. & Roeper, J. Ih channels contribute to the different functional properties of identified dopaminergic subpopulations in the midbrain. *Journal of Neuroscience* **22**, 1290-1302 (2002).

25 Gastrein, P. *et al.* The role of hyperpolarization-activated cationic current in spike-time precision and intrinsic resonance in cortical neurons in vitro. *The Journal of physiology* **589**, 3753-3773 (2011).

26 Mansouri, A., Fallah, A. & Valiante, T. A. Determining surgical candidacy in temporal lobe epilepsy. *Epilepsy research and treatment* **2012** (2012).

27 Kostopoulos, G., Drapeau, C., Avoli, M., Olivier, A. & Villemeure, J. G. Endogenous adenosine can reduce epileptiform activity in the human epileptogenic cortex maintained in vitro. *Neuroscience letters* **106**, 119-124 (1989).

28 Köhling, R. & Avoli, M. Methodological approaches to exploring epileptic disorders in the human brain in vitro. *Journal of neuroscience methods* **155**, 1-19 (2006).

29 Ting, J. T., Daigle, T. L., Chen, Q. & Feng, G. in *Patch-Clamp Methods and Protocols* 221-242 (Springer, 2014).

30 Gouwens, N. W. *et al.* Classification of electrophysiological and morphological neuron types in the mouse visual cortex. *Nature neuroscience* **22**, 1182-1195 (2019).

31 Poorthuis, R. B. *et al.* Rapid neuromodulation of layer 1 interneurons in human neocortex. *Cell reports* **23**, 951-958 (2018).

32 Bar-Yehuda, D. & Korngreen, A. Space-clamp problems when voltage clamping neurons expressing voltage-gated conductances. *Journal of neurophysiology* **99**, 1127-1136 (2008).

33 Hutcheon, B., Miura, R. M. & Puil, E. Subthreshold membrane resonance in neocortical neurons. *Journal of Neurophysiology* **76**, 683-697 (1996).

34 McInnes, L., Healy, J., Saul, N. & Grossberger, L. UMAP: Uniform Manifold Approximation and Projection. *Journal of Open Source Software* **3**, 861, doi:10.21105/joss.00861 (2018).

35 Higgs, M. H. & Spain, W. J. Conditional bursting enhances resonant firing in neocortical layer 2–3 pyramidal neurons. *Journal of Neuroscience* **29**, 1285-1299 (2009).

36 Galán, R. F., Ermentrout, G. B. & Urban, N. N. Optimal time scale for spike-time reliability: theory, simulations, and experiments. *Journal of neurophysiology* **99**, 277-283 (2008).

37 Neske, G. T. & Connors, B. W. Distinct roles of SOM and VIP interneurons during cortical up states. *Frontiers in neural circuits* **10**, 52 (2016).

38 Benjamini, Y. & Hochberg, Y. Controlling the false discovery rate: a practical and powerful approach to multiple testing. *Journal of the royal statistical society. Series B (Methodological)*, 289-300 (1995).

39 Bates, D., Mächler, M., Bolker, B. & Walker, S. Fitting Linear Mixed-Effects Models Using lme4. *Journal of Statistical Software* **67**, 48, doi:10.18637/jss.v067.i01 (2015).

40 Burnham, K. P. & Anderson, D. R. Multimodel inference: understanding AIC and BIC in model selection. *Sociological methods & research* **33**, 261-304 (2004).

41 Berg, J. *et al.* Human cortical expansion involves diversification and specialization of supragranular intratelencephalic-projecting neurons. *BioRxiv* (2020).

42 Hutcheon, B. & Yarom, Y. Resonance, oscillation and the intrinsic frequency preferences of neurons. *Trends in neurosciences* **23**, 216-222 (2000).

43 Zemankovics, R., Káli, S., Paulsen, O., Freund, T. F. & Hájos, N. Differences in subthreshold resonance of hippocampal pyramidal cells and interneurons: the role of h-current and passive membrane characteristics. *The Journal of physiology* **588**, 2109-2132 (2010).

44 Ramaswamy, S. & Markram, H. Anatomy and physiology of the thick-tufted layer 5 pyramidal neuron. *Frontiers in cellular neuroscience* **9**, 233 (2015).

45 Baker, A. *et al.* Specialized subpopulations of deep-layer pyramidal neurons in the neocortex: bridging cellular properties to functional consequences. *Journal of Neuroscience* **38**, 5441-5455 (2018).

46 Hodge, R. D. *et al.* Conserved cell types with divergent features in human versus mouse cortex. *Nature* **573**, 61-68 (2019).

47 Akam, T. & Kullmann, D. M. Oscillations and filtering networks support flexible routing of information. *Neuron* **67**, 308-320 (2010).

48 Yu, X. & Lewis, E. R. Studies with spike initiators: linearization by noise allows continuous signal modulation in neural networks. *IEEE Transactions on Biomedical Engineering* **36**, 36-43 (1989).

49 Padmanabhan, K. & Urban, N. N. Intrinsic biophysical diversity decorrelates neuronal firing while increasing information content. *Nature neuroscience* **13**, 1276 (2010).

50 Ulrich, D. Dendritic resonance in rat neocortical pyramidal cells. *Journal of neurophysiology* **87**, 2753-2759 (2002).

51 Dembrow, N. C., Chitwood, R. A. & Johnston, D. Projection-specific neuromodulation of medial prefrontal cortex neurons. *Journal of Neuroscience* **30**, 16922-16937 (2010).

52 Schmidt, S. L., Dorsett, C. R., Iyengar, A. K. & Fröhlich, F. Interaction of intrinsic and synaptic currents mediate network resonance driven by layer V pyramidal cells. *Cerebral Cortex* **27**, 4396-4410 (2016).

53 Lampl, I. & Yarom, Y. Subthreshold oscillations and resonant behavior: two manifestations of the same mechanism. *Neuroscience* **78**, 325-341 (1997).

54 Carracedo, L. M. *et al.* A neocortical delta rhythm facilitates reciprocal interlaminar interactions via nested theta rhythms. *Journal of Neuroscience* **33**, 10750-10761 (2013).

55 Chagnac-Amitai, Y., Luhmann, H. J. & Prince, D. A. Burst generating and regular spiking layer 5 pyramidal neurons of rat neocortex have different morphological features. *Journal of Comparative Neurology* **296**, 598-613 (1990).

56 Perin, R., Berger, T. K. & Markram, H. A synaptic organizing principle for cortical neuronal groups. *Proceedings of the National Academy of Sciences* **108**, 5419-5424 (2011).

57 Florez, C. *et al.* In vitro recordings of human neocortical oscillations. *Cerebral Cortex* **25**, 578-597 (2013).

58 Habib, N. *et al.* Massively parallel single-nucleus RNA-seq with DroNc-seq. *Nature methods* **14**, 955 (2017).

978

979 Supplemental Figures and Legends

980

981

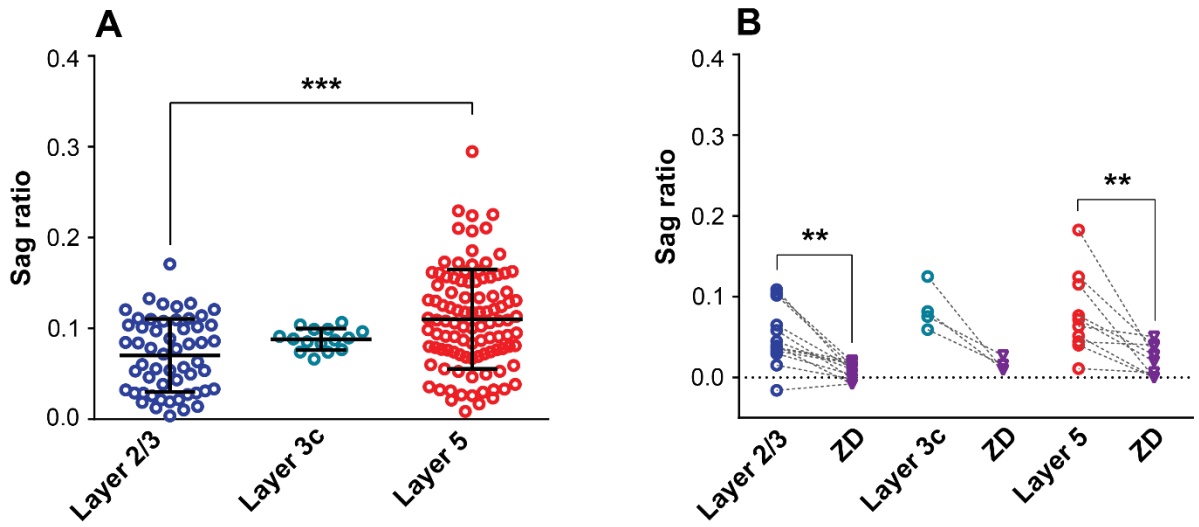

982

983 **Figure S1: Sag differences between cortical layers are robust to normalizing for input resistance differences**
984 **using the dimensionless sag ratio mesaure. (A)** Same as Fig 2B, but data are plotted using the sag ratio
985 measure. **(B)** Same as Fig 2E, showing bath application of I_h blocker ZD7288 (10 μM) reducing sag ratio in
986 pyramidal cells from both layers.

987

988

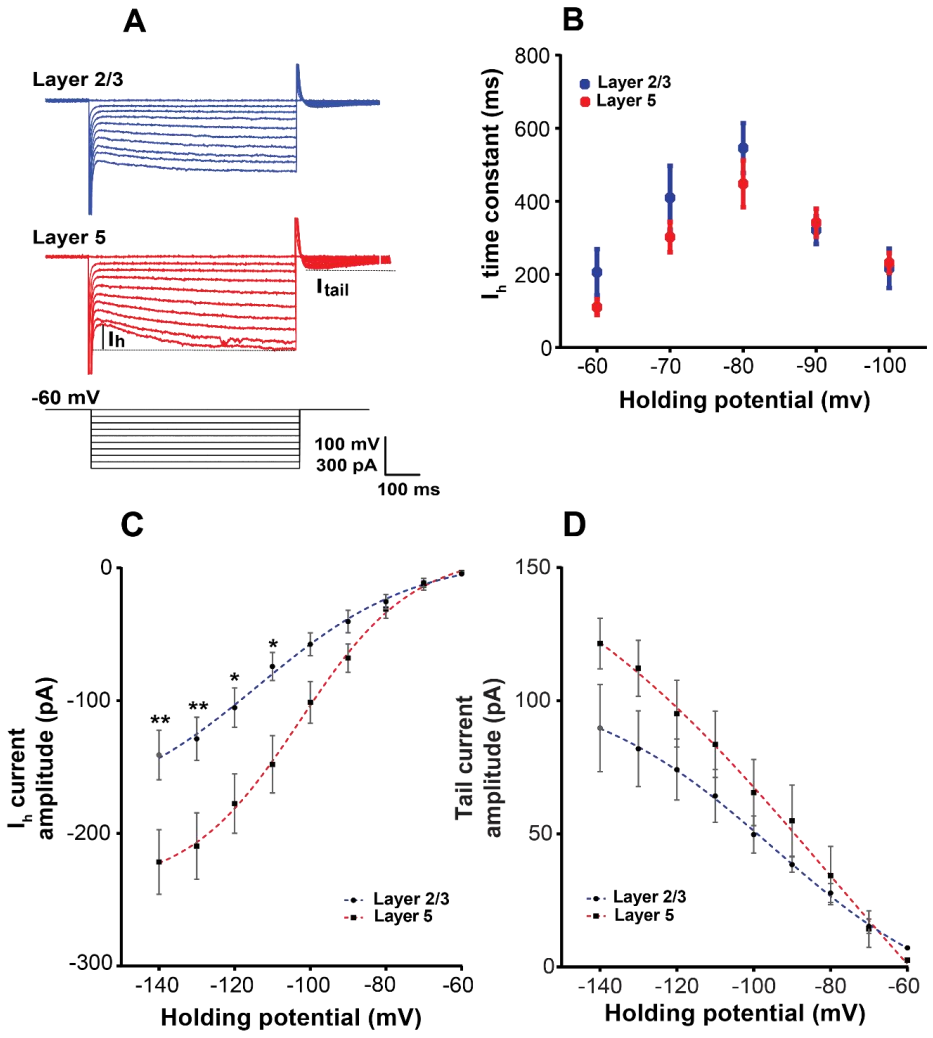

Figure S2: The kinetics of I_h are similar between L2/3 and L5 pyramidal cells. (A) Example voltage-clamp recordings of L2/3 and L5 pyramidal cells. Annotations show calculation of I_h and I_{tail}. **(B)** Voltage clamp recordings of current show that I_h time constants are similar between L2/3 and L5 pyramidal cells. **(C)** L5 pyramidal cells had significantly larger amplitude I_h compared to L2/3 pyramidal cells. **(D)** Quantification of I_{tail} at the end of each holding potential revealed that there was no significant difference between L2/3 and L5. The dashed lines in **C** and **D** indicates the fit to a Boltzmann function. These data suggest that the difference between sag voltages in L2/3 and L5 pyramidal cells are not due to differences in the kinetics of HCN channels.

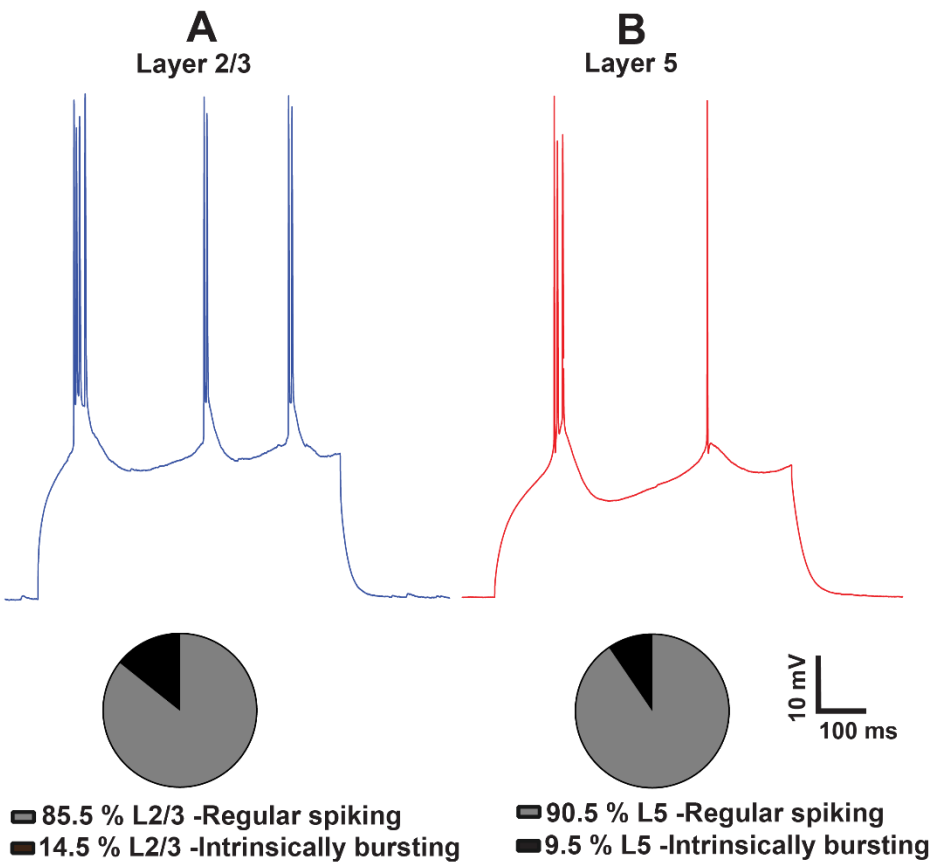

Figure S3: Distribution of different firing patterns across L2/3 and L5 pyramidal cells. (A,B) Example voltage traces of intrinsically bursting neurons at rehobase. L2/3 (A) and L5 (B) pyramidal cells tend to have more regular spiking than intrinsically bursting neurons.The percentage of intrinsically bursting neurons recorded in L2/3 was slightly higher than L5.

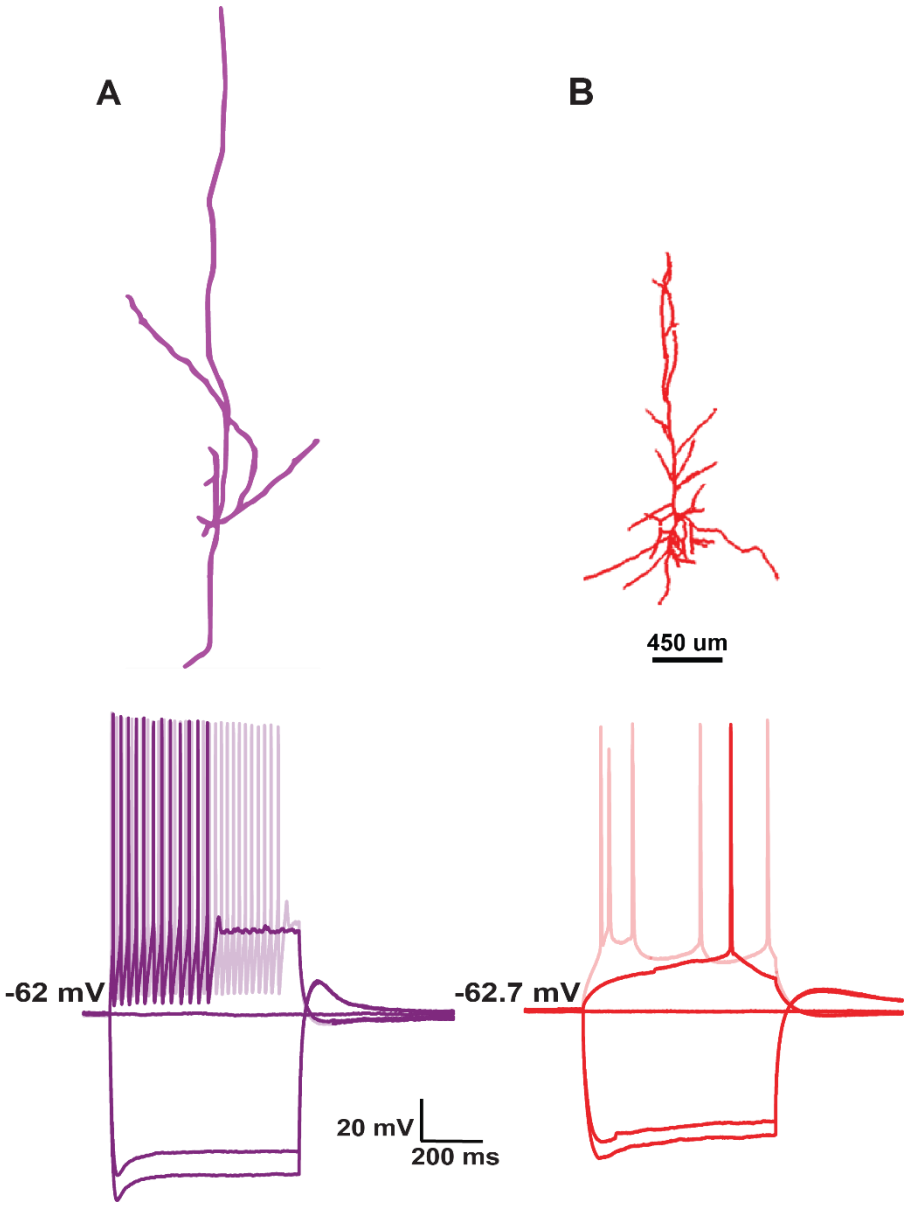

Figure S4: Morphological evidence for interneuron sampling. **(A)** Morphological reconstruction and firing pattern following hyperpolarizing and depolarizing current injections for a putative interneuron. **(B)** Morphological reconstruction from a confirmed pyramidal cell (cell f in Figure 1) and related firing pattern following hyperpolarizing and depolarizing current injections.

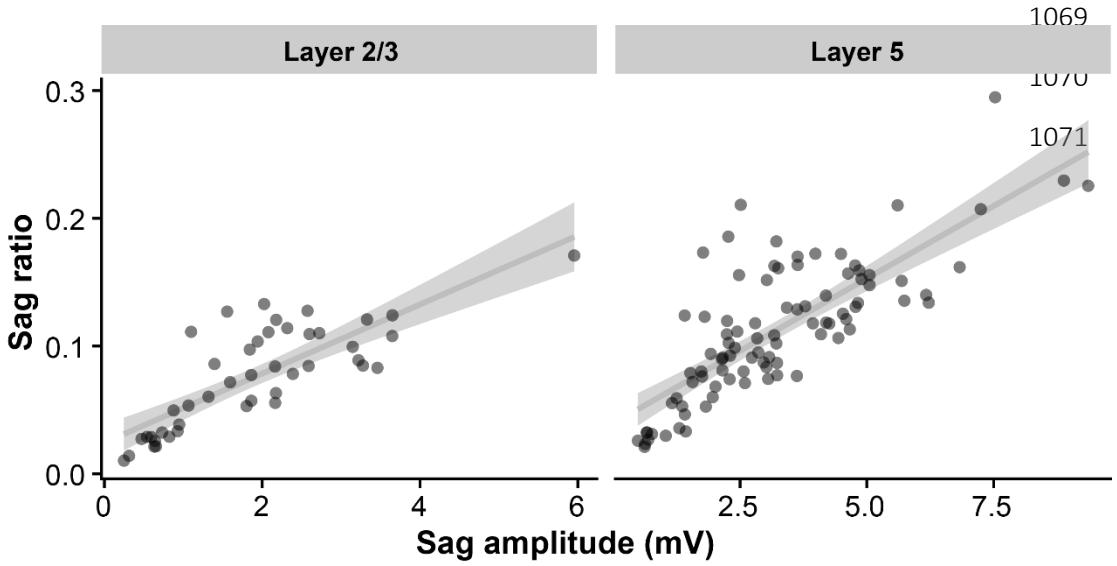

Figure S5: Correlation between sag voltage and sag ratio in data from the Krembil Institute cohort.

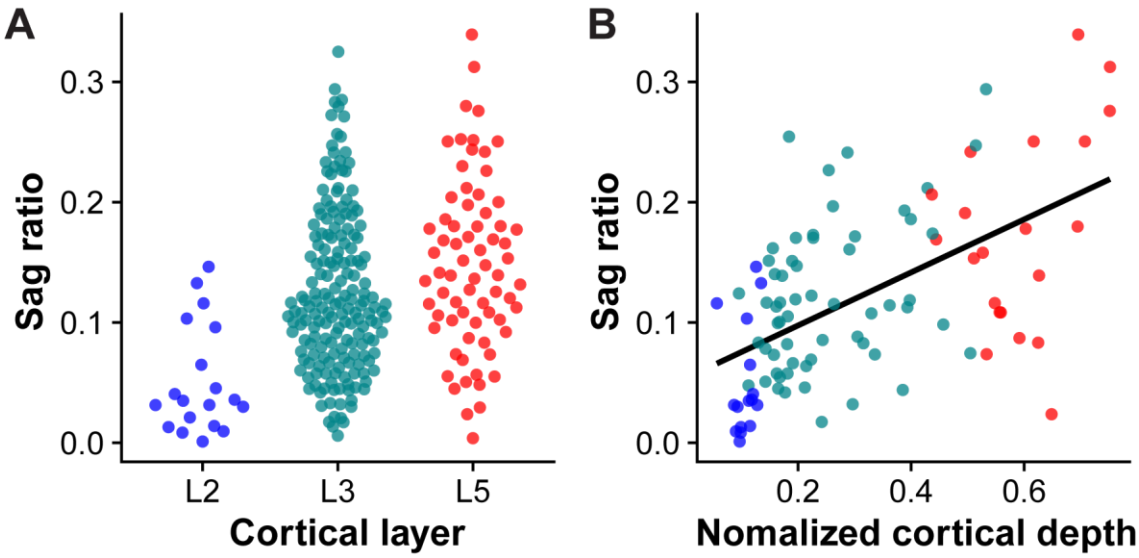

Figure S6: Sag ratio measurements in human cortical pyramidal cells collected from the Allen Institute. (A) Sag ratio measurements collected in each cortical layer. **(B)** Sag ratio as a function of normalized cortical depth from the pial surface. Cells are a subset of those shown in (A) with normalized cortical depth information available. Line indicates best fit line.

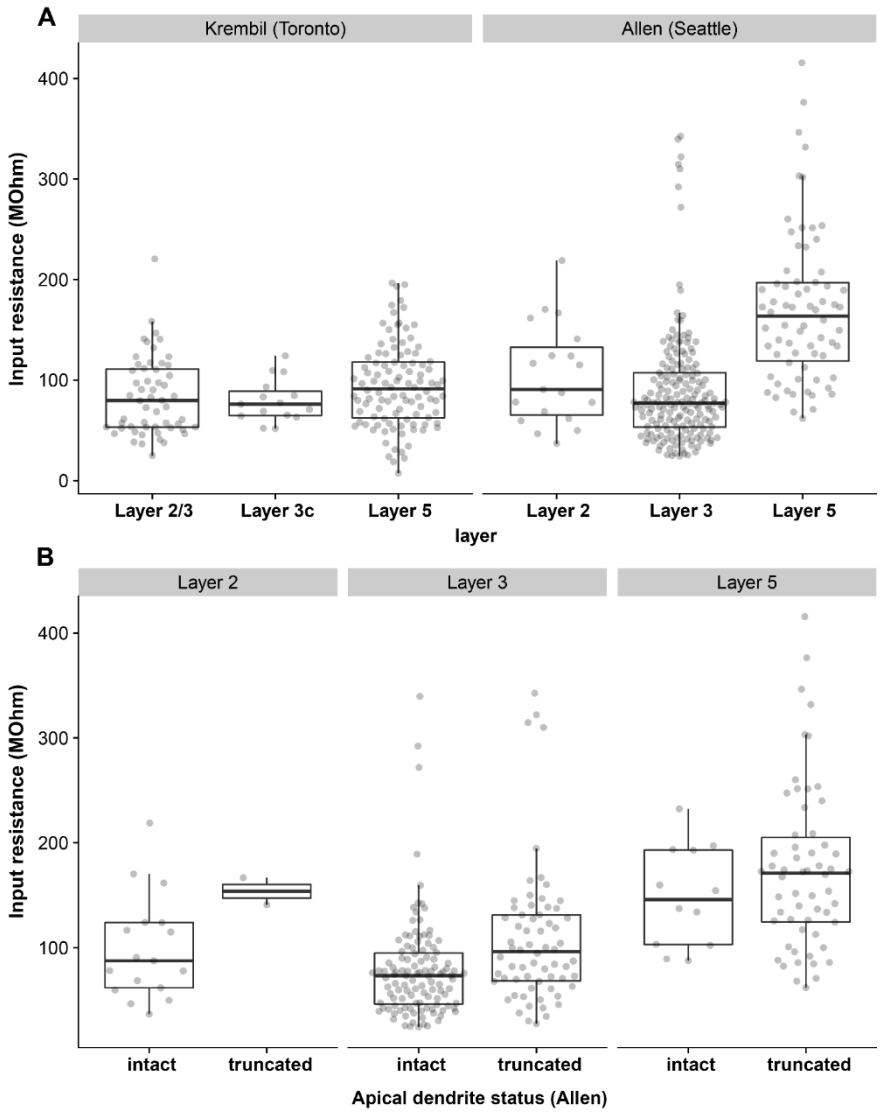

Figure S7: Comparison of input resistance measurements in human cortical pyramidal cells collected from the Krembil Institute and the Allen Institute. (A) Input resistance measurements from Krembil Institute cohort (left) and Allen Institute cohort (right). Note trend for increase in input resistances from L5 pyramidal cells relative to L2/3 neurons. **(B)** Same as right panel of B, but data have been grouped by whether the apical dendrite is intact or truncated. According to Allen Institute's documentation, an apical dendrite is "intact" if the entire length of the primary dendrite was contained within the thickness of the slice and "truncated" if the primary dendritic branch was cut off at either slice surface. While dendrite truncation tends to increase input resistances, the overall relationship that input resistances in L2/3 are smaller than in L5 holds for neurons with confirmed intact primary dendrites.

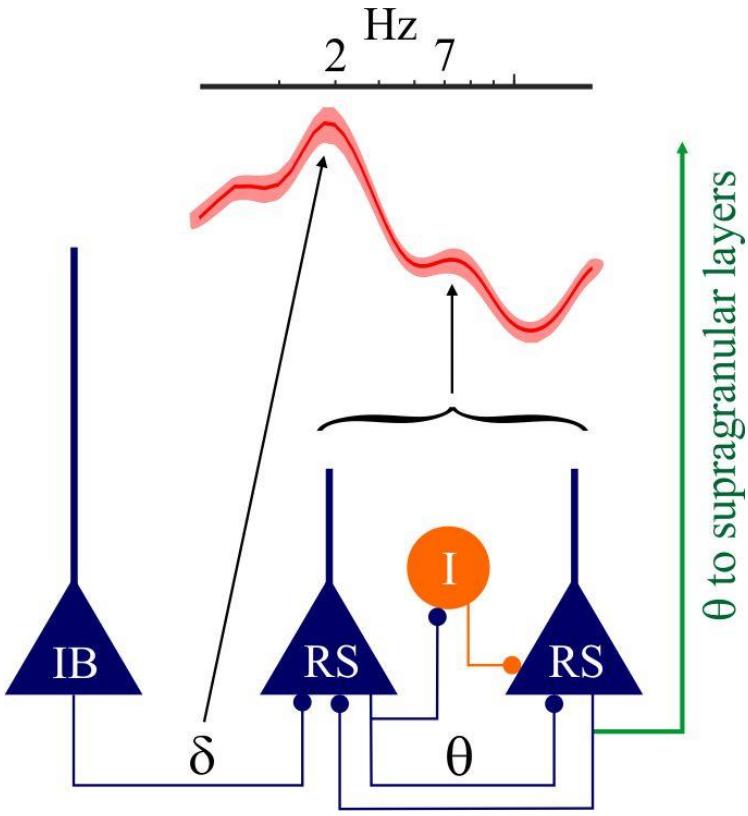

Figure S8: Structural circuit motif for L5 theta oscillations. Delta frequency output from intrinsically bursting (IB) [54] neurons is well tracked by regular spiking (RS) neurons that have a peak in *G(f)* (red) (see Figure 7B in main text) within the delta frequency range. In turn RS neurons that are poorly adapting, have steep f-I curves, and low rheobase discharge at theta frequency [54]. RS cell drive local circuits at theta frequency range including other RS neurons that track theta well via the peak at 7Hz in G(f). Interneurons amplify local activity through rebound excitation (I; orange; see Figure 5 main text) in human circuits that are predisposed to reverberant activity [7].